4

Single-atom catalysts for biomass-derived drop-in chemicals

Pawan Kumar, M.A. Khan, Jinguang Hu, Md. Golam Kibria

DEPARTMENT OF CHEMICAL AND PETROLEUM ENGINEERING, UNIVERSITY OF CALGARY, CALGARY, AB, CANADA

4.1 Introduction

If there is anything the year 2020 has taught us is that, if we human beings do not take responsibility for our actions and take corrective measures, then mother nature will take matters into its own hands which could be catastrophic for us. There are a few numbers that highlight how much human activities have impacted the environment around us. Since 1850, 950 gigatons of CO_2 from human activity went into the atmosphere. If the oceans did not come to our rescue, the number would have been close to 2,400 gigatons of CO_2 [1]. This had led to an increase in the concentration of carbon dioxide in the Earth's atmosphere from around 275 parts per million (ppm) before the Industrial Revolution to over 419 ppm in June 2021, causing global warming and resulting in a damaging effect on the environment [1,2]. At the current pace of CO_2 emissions, the global temperatures are expected to rise by $\sim$4.8°C by the year 2100, which is a scary scenario [3]. The effect of global warming is becoming more evident and visible in the form of melting of glaciers (thawing of the Arctic permafrost), increased sea levels, frequent extreme events, and endangered biodiversity [4–7]. In 2018, the world was shocked when an iceberg (B-46, size: 115 square miles), five times the size of Manhattan was broken in Pine Island Glacier in West Antarctica [8]. In other news, the Arctic's strongest sea ice is breaking up for the first time and will have been pushed away from the coast to an area where it will melt more quickly.

And what is more worrying is that we are still heading in the wrong direction. Despite all the good intentions and the signing of the Paris Agreement in 2016, emissions are still going up. In 2019, about 43.1 billion tons of CO_2 from anthropogenic activities were emitted into the atmosphere. It was an all-time high, breaking the previous record from 2018 [1]. According to the UN Environment Program, emissions must fall by 25% before 2030 to keep temperature increase within 2°C by 2100 and 55% reductions are needed by 2030 to limit the increase to 1.5°C [1]. We need a huge shift in energy policies to maximize energy production/use from renewables and work on technologies for carbon capture, conversion, and utilization and storage (CCUS) [9–11]. In the last decade, there has been tremendous progress

Advanced Catalysis for Drop-in Chemicals. DOI: https://doi.org/10.1016/B978-0-12-823827-1.00009-2

in efficient harvesting renewable energy from sunlight and wind and CCUS technologies. It is amazing to think that plants and trees have been doing this very job for us for millions of years, that is, harvesting sunlight and capturing CO_2 to convert to energy (photosynthesis), in what we call biomass energy. Human beings have been using this energy from biomass for thousands of years via burning of forestry materials and agricultural waste biomass [12]. Indeed, energy from traditional biofuels remains the largest source of renewables, accounting for 60%−70% of renewable energy use [12]. Bio-based renewables are carbon neutral and can be easily integrated into current energy systems. Plants harvest solar energy in the chemical bond of biomolecules which can be later used for energy production. The entire human population consumes 12.2 billion tons (equivalent 101 million barrels) of crude oil in a year (2019), while the Earth receives 90,000 billion tons of oil equivalent solar energy in one year [13−15]. So all the energy humanity needs in an entire year can be supplied by collecting sunlight for an hour. Plants can capture almost 72 billion tons of oil-equivalent energy in the form of biomass which means one-sixth of biomass can supply our entire energy demand [16,17].

In the past few years, there has been a lot of focus on developing materials and technologies for sustainable conversion and the use of biomass energy by converting it into fuels and value-added chemicals. A sustainable economy where we depend on biomass energy is depicted in Fig. 4−1, where we need to make the transition from a traditional hydrocarbon-based "oil-refinery" to a more sustainable biomass-based "bio-refinery" platform. Biomass can be used to produce biofuel which currently represents only a total of 1.2%−2.0% of renewables [18]. Bio-derived chemicals are equivalent to their petrochemical molecules regardless of their origin, however, they have lower carbon footprints and can be used as

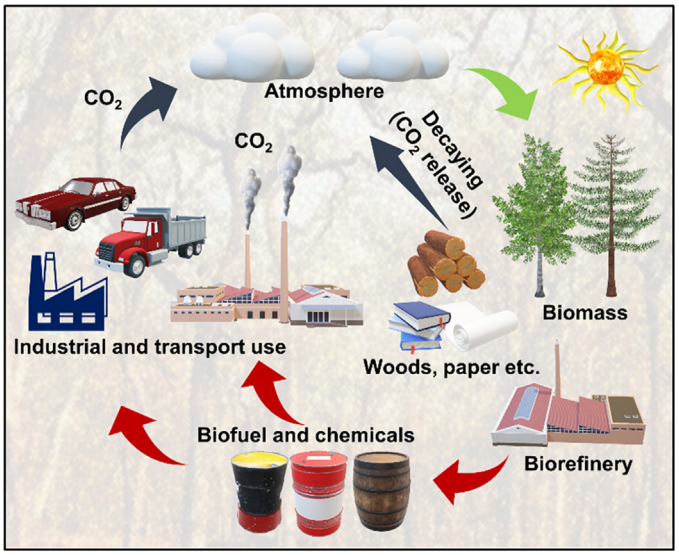

FIGURE 4–1 Sustainable conversion of biomass into fuel and value-added chemicals.

drop-in chemicals and fuel additives [19]. The term "drop-in chemicals" is used for large volume commodity chemicals and polymers, and bio-derived drop-in chemicals represent bio-versions of existing petrochemicals identical to existing fossil-based chemicals [20]. Current bio-based drop-in chemicals are more expensive compared to their fossil counterparts due to less mature catalytic and processing technologies. The conventional first generation of biofuels and chemicals were produced from sugary, starchy, and fatty oil-rich crops [21]. For instance, a wide variety of starchy crops such as sugarcane (Brazil), wheat, and sugar beets (Europe), corn (United States), cassava, potato, rice, oats, grapes, and other fruits were used for bioethanol production via fermentation. As per the regulations, it is mandatory to blend 10% ethanol into gasoline fuel. Similarly, biodiesel, a long-chain fatty acid ester prepared by transesterification of fatty acids with alcohol (usually methanol), was produced from fatty acid-rich biomass. The debate on "food versus fuel" criticizes the use of wide arable land and food crops just for the production of fuel, which now widely accepted is that first-generation biofuels cannot completely replace fossil fuels [22]. To overcome these issues, researchers are looking to develop second-generation biofuels that can convert lignocellulose biomass in nonedible plant matter, waste vegetable oils, and agricultural wastes to fuels and chemicals [23,24].

Lignocellulose is composed of cellulose (by polymerization of glucose), hemicellulose (a polymer of glucose and xylose), and lignin (cross-linked polymer built of substituted phenols) [25]. Cellulose represents the largest fraction of renewable biomass produced via photosynthesis (22×10^9 tons annually); an actual estimated annual production of 7.5×10^{10} tons [26,27]. Approximately 4×10^9 ton/year cellulose derived from wood (timbers), grass, sugarcanes, etc., are readily available for the production of fuel and chemicals. Nonfood crops such as switchgrass and giant miscanthus can be used as energy crops [28]. Therefore, it is desirable to use lignocellulosic biomass as feedstock. The various reaction pathways for renewable fuels and chemicals that can be obtained from lignocellulosic biomass are summarized in Fig. 4−2. Currently, there are two major biomass valorization platforms, employing either thermochemical or biological processes. Thermochemical processes such as pyrolysis are the preferred conversion method for biomass to liquids [30−32]. Thermal pyrolysis and fractionation of lignocellulosic biomass allow easy processing of C5 and C6 sugars in biomass to convert them into important platform chemicals such as furfural, hydroxy-methyl-furfural (HMF), and levulinic acid. A recently developed biphasic system that includes acidic treatment followed by an organic solvent such as 2-sec-butylphenol has increased yields of platform chemicals [29]. However, the requirement of harsh acidic/basic condition to breakdown the recalcitrant cell walls of the lignocellulosic (polymer-lignin-hemicellulose) biomass makes the process costly. Additionally, the major fraction of cellulose present in the cell is highly crystalline such as cellulose nanocrystals and cellulose nanofibers [33]. The biomass feedstocks are usually rich in oxygen and moisture contents that results in the production of thermally unstable and oxygenated chemicals. The deoxygenation of these oxygenated chemicals involve the removal of oxygen as water, producing high-value chemical feedstocks that can substitute petroleum or petroleum-derived chemicals [34]. While thermochemical processes for biomass conversion can produce biofuels, chemicals,

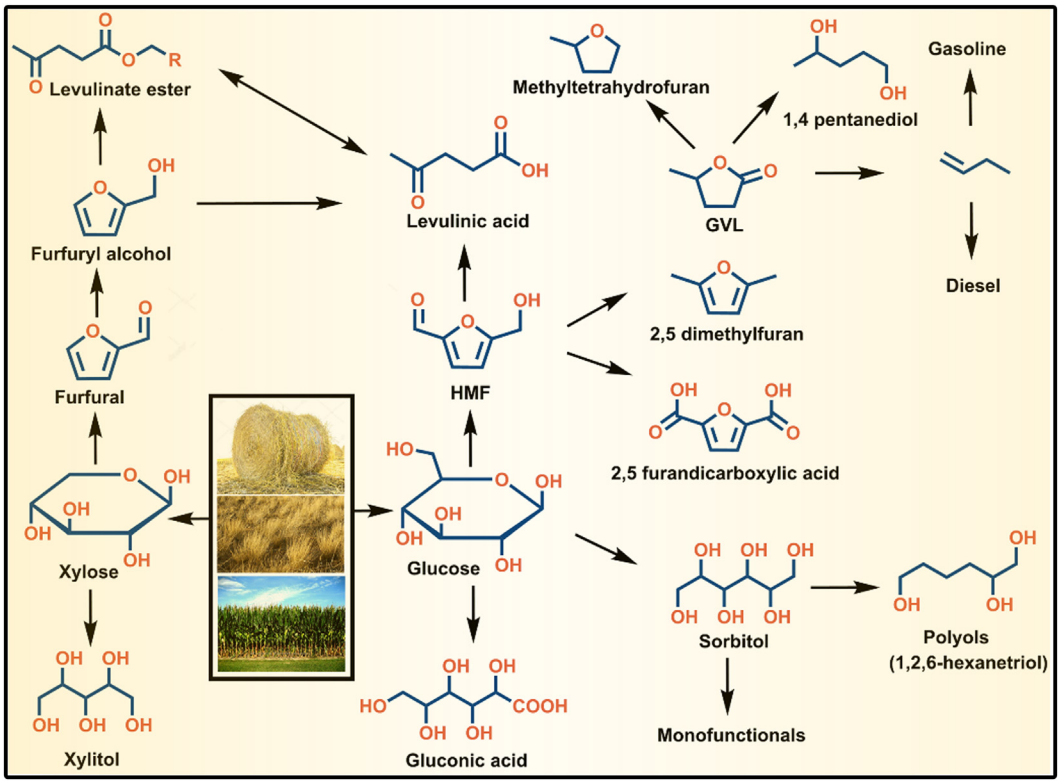

FIGURE 4–2 Reaction pathways for renewable fuels and chemicals from lignocellulosic biomass [29]. *Adapted with permission from S.G. Wettstein, D.M. Alonso, E.I. Gürbüz, J.A. Dumesic, A roadmap for conversion of lignocellulosic biomass to chemicals and fuels, Curr. Opin. Chem. Eng., 1 (2012) 218–224. Copyright 2012 Elsevier.*

and generate power, they are carbon and energy-intensive processes. Large scale processes to convert biomass to fuels and commodity chemicals will rely on efficient catalytic systems which can make the biorefinery concept sustainable. The key challenge for the bio-refinery platform will be the development of efficient catalytic systems that can selectively transform bio-derived organic molecules into valuable commodity chemicals.

Several catalytic systems have been widely investigated for biomass valorization and upgrading biomass to renewable chemicals and fuels [35–37]. A plethora of micro/mesoporous material with uniform pore size distribution such as zeolites, MCM-41, MSU with mono- and bifunctional catalytic sites have been studied for catalytic biomass conversion [38]. The presence of acidic, basic, or bifunctional sites play a crucial role in product formation. For example, H-ZSM-5 (a zeolite with the structure code MFI) promotes deoxygenation, decarboxylation, and decarbonylation, protolytic cracking or β-scission, alkylation, isomerization, cyclization, oligomerization and aromatization reactions of bio-mass catalyzed by acidic sites via a carbonium ion mechanism [39,40]. However, coke deposition and tar formation are challenging issues which are temporarily overcome by burning coke at high temperatures in

the air. As the conversion of biomass involves the removal of oxygen contents of bio-derived products via deoxygenation, hydrodeoxygenation, hydrogenation, and hydrogenolysis/dehydroxylation, noble metal-catalyst envisages as promising catalysts. Noble metal, due to their innate affinity to hydrogen adsorption and high specific surface energy, can promote a variety of reactions such as hydrogenation and deoxygenation. Furthermore, the activity can be boosted by the deposition of noble and transition metals on micro/mesoporous hybrid materials such as activated carbon, mesoporous clay, and zeolites. Unfortunately, the limited abundance of noble metals in earth and high cost restrict their application. To subside the noble metals, abundant transition metals such as nickel (Ni) and cobalt (Co) deposited on zeolites (ZSM-5) are also used for upgrading biomass pyrolysis products [41]. Alloy and bimetallic catalysts were also found to improve overall conversion efficiency. Some transition metal carbides (an interstitial alloy of metal and carbon with C:N < 0.59) have shown noble metal-like properties especially in hydrogenation reactions, which stimulated hope to develop inexpensive catalysts with similar properties [42]. Indeed, a few metal carbides such as W_2C and Mo_2C displayed platinum-like properties (sometimes better) and promote biomass conversion by C—C, C—O—C, and C—O—H bonds cleavage more specifically for the hydrogenation reactions [43]. However, due to the high oxygen content in biomass feedstocks, the presence of multiple components requiring different reaction conditions, low selectivity due to side reactions, and catalyst poisoning under operating conditions, most of the catalysts display poor performance in biomass conversion [44,45]. The effective distribution of specific catalytic centers and the maximization of the number of catalytic sites are the keys to designing more active and product selective catalysts. During past decades, numerous catalytic systems with a fine distribution of transition metal on active supports have been reported, however, controlling the size and nature of catalytic sites remains challenging. Single-atom catalysts (SACs) are new frontiers in catalysis due to their exceptional selectivity, reactivity, and recyclability. The availability of every single-atom and their specific stabilization on active support enhance catalytic activity and selectivity. Combined with the two most significant attributes: (1) high activity like in homogenous catalysts, and (2) better recyclability like in heterogeneous catalysts, SACs can solve the aforementioned issues. The next sections are a detail discussion on SACs and their applications in biomass conversion.

4.2 Single-atom catalysts

In recent years, single-atom catalysts (SACs) have emerged as a promising class of material to target catalytic reactions that traditionally suffer from low selectivity such as biomass conversion. SACs contain isolated individual atoms dispersed on the surface of appropriate supports and provide an alternative strategy to tune the activity and selectivity of catalytic reactions. Noble metals such as Pd, Pt, Ru, Rh, Au, Ag, etc. are superior heterogeneous catalysts that are traditionally used in the petrochemical industry due to their exceptional reactivity. However, limited abundance and high cost make it essential to downsize catalysts economically. Transformation of bulk materials into nano-regime (1−100 nm) increases the

performance of catalysts because the exposed catalytic site at the edge of nanoparticles works as a catalytic center. The physical, chemical, mechanical, and optoelectronic properties of nanoparticles are highly size-dependent; in the size range of 1−10 nm (nanoclusters), the nanoparticles (NPs) display entirely different properties than bulk and individual atoms. Such changes are observed due to the change in the geometric and energic state due to the discretization of orbitals.

Further, reduction of metal size below the sub-nano regime (in atomic-scale $\approx$ Å range) tremendously alters the catalytic performance due to the low-coordination environment of metal atoms, increased surface energy, high atom utilization, and improved strong metal-support interactions. SACs bridge the gap between homogenous and heterogeneous catalysis by offering ultimate atom utilization due to accessibility of each active site, like homogeneous catalysts, while preventing leaching of metal-like heterogeneous catalysts, resulting in better selectivity and cost reduction [46,47]. The specific electronic and geometric configuration, due to the absence of M-M bonds and presence of the cationic (or sometimes anionic) catalytic sites, provides unique and tunable selectivity for an SAC [48,49]. For example, Pt_1/FeO_x SACs promotes the chemo-selective reduction of 3-nitrostyrene while neither pure Fe_2O_3 support nor the Pt_1/FeOOH-RT were active at all for the reaction [50]. Moreover, lowering the coordination number of Pt-O led to a lower oxidation state of Pt single-atoms and a higher catalytic activity.

Additionally, by tuning the structural attributes of support, the nature and spatial distribution of metal centers can be controlled to achieve 100% selectivity like an enzyme [51]. Since the first report of Tao Zhang in 2011 on the synthesis of isolated Pt single-atoms on FeO_x nano-crystallites for CO oxidation, numerous SACs have been developed [52]. The metal atom can catalyze a reaction either individually or coordinate with supporting material to get activated. When a single-atom is stabilized on the second metal surface, single-atom alloy (SAA) is the preferred terminology [53]. While mentioning SACs, It should be strictly understood that they are comprised of isolated single atoms free of small organic ligands on a supporting material and do not include gaseous metal atoms or homogeneous metal complexes on any surface, such as silicate or zeolites. However, the removal of organic ligands can afford monoatomic SACs. So the later homogenous metal complex supported on zeolites are an example of a single-site heterogeneous catalyst (SSHC), which possess identical catalytically active sites dispersed on a solid surface [54]. Contrary to SSHC, in SACs not all the catalytic sites are identical due to surface heterogeneity of the supporting matrix. Despite the observed performances for various reactions, significant challenges associated with the synthesis, stabilization, and application of SACs exist as well. A major challenge in the synthesis of SACs is to precisely control and determine the coordination environment of the single-atoms. The coordination affects the electronic environment which concomitantly affects reactivity and selectivity. Another key challenge in the application of SACs is the stabilization of isolated metals on supports without compromising catalytic activity, especially at high temperatures or under harsh reaction conditions. (Fig. 4−3)

Various methods, such as impregnation, photochemical reduction, high-temperature trapping, atomic layer deposition, and pyrolysis of metal organic frameworks (MOFs) have

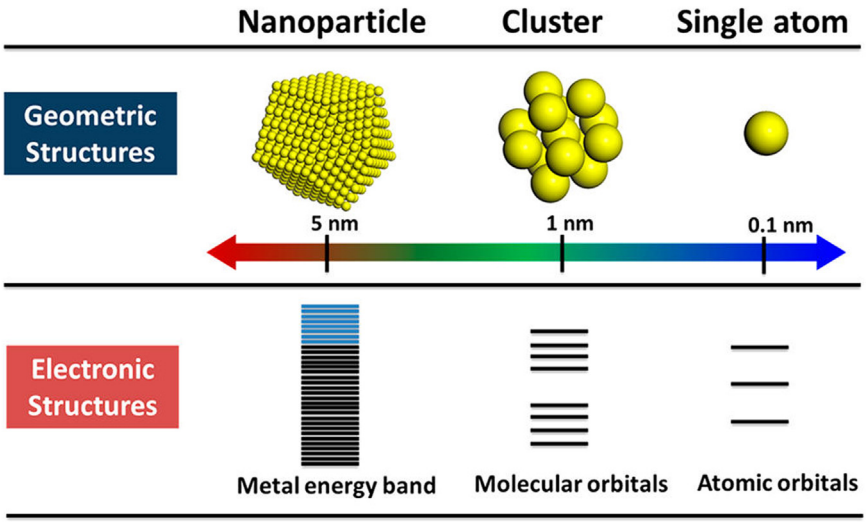

FIGURE 4–3 Geometric and electronic structures of single-atom, clusters, and nanoparticles [55]. *Reproduced with permission from L. Liu, A. Corma, Metal catalysts for heterogeneous catalysis: from single-atoms to nanoclusters and nanoparticles, Chem. Rev., 118 (2018) 4981−5079. Copyright 2012 American Chemical Society.*

been used to prepare SACs [56−60]. Many supports such as metal oxides (TiO_2, ZnO, ZrO_2, FeO_x), metal nitrides (TiN), phosphomolybdic acid, etc., have been used for the fabrication of SACs [61−65]. The most commonly used supports for the fabrication of single-atom catalysts are oxides due to a high specific surface area, the presence of plenty of oxygen/metal vacancies, and surface oxygens (-OH) that stabilize the single metal atoms [58,66]. The strong metal-support interaction helps in improving thermal stability at elevated operating temperatures. In recent years, two-dimensional (2D) materials have also emerged as excellent supporting materials to fabricate SACs because of their high surface area, excellent conductivity, and the possibility of chemical functionalization [67−69]. The incorporation of single-atoms in the framework of 2D materials can lead to synergistically improved performance due to the stabilization of single-atom via coordination and charge transfer between 2D materials and a single-atom. Numerous 2D materials such as MoS_2, WS_2, and MXenes (i.e., Ti_3C_2) have been used for the synthesis of SACs [70−75]. Recently, graphitic carbon nitride (g-C_3N_4), a 2D polymer, constituted of tris-*s*-triazine (heptazine) units linked together with tertiary amine, has emerged as an ideal candidate to fabricate SACs due to its intriguing chemical, physical, and optical properties [8,14,76]. Carbon nitride-based SACs can be synthesized at low temperatures and have high metal loading due to the accommodation of metals in the in-plane cavities via coordination with N atoms [77−79]. Although many SACs fabricated on various supports have already been gaining popularity for the synthesis of fine chemicals, only limited reports are available on their applications in biomass transformations. In the next sections, we will review the work done on developing SACs for important catalytic conversion of biomass and its derived molecules.

4.3 Single-atom catalysts for biomass utilization

4.3.1 Hydrodeoxygenation of furfuryl alcohol to 2-methylfuran

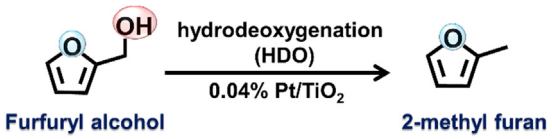

The hydrodeoxygenation (HDO) of lignocellulosic biomass via hydrogenation and cleavage of specific C—O bonds is an attractive reaction to achieve a sustainable carbon-neutral economy [80,81]. Noble metals are excellent hydrogenation catalysts, however, they promote nonselective hydrogenation of C═C bonds resulting in ring hydrogenation and ring-opening reactions (ring chemistry) of furan and aromatic rings of biomaterials [82,83]. On the other hand, metal oxides are highly active and selective toward C═O hydrogenation and cleavage of hydroxyls group attached to rings without ring chemistry [84]. The selective C—O bond cleavage via the reverse Mars—van Krevelen mechanism takes place on hydrogen-generated oxygen vacancies as active redox centers, and surface oxygen is regenerated via C—O bond scission for the continuation of the catalytic cycle [85]. The rates of C—O bond cleavage for oxygen regeneration and oxygen vacancy generation via H_2 should be equilibrated to get a robust catalyst. The more reducible metal oxide enhances catalytic activity due to increased numbers of vacancies; however, it renders the oxide less stable towards reduction. Previous studies based on temperature programmed reduction (TPR) show a decrease of reduction temperature on noble metal-metal oxides [86]. Further, noble metals and reducible metal oxides can also work synergistically for improving the activity and selectivity for the deoxygenation of various biomass-derived substrates [87,88]. So a metal oxide surfaces doped with noble metals should be an ideal catalyst to increase the surface activity and HDO turnover number, by promoting the formation of vacancies and redox centers without compromising bulk stability. Distinguishably, the use of a metal single-atom catalyst can further enhance the turn over frequency (TOF) and selectivity of the reaction.

Fu et al. demonstrated that atomically dispersed Pt-doped TiO_2 with an ultralow-loading of Pt (0.04%) could selectively transform furfuryl alcohol (FA) to 2-methylfuran (2MF) [89]. The FA was chosen as a model substrate for the reaction because of its structural similarity with 5-hydroxymethylfurfural (HMF), a furan derivative produced from sugar valorization. Based on DFT, the hydrogen-assisted Gibbs energy for vacancy formation for Pt doped TiO_2 was calculated by considering five and six oxygen atom coordinations for Pt. As (101) facet of TiO_2 was predominated (97% surface) and doped Pt mainly catalyzes the reaction in comparison to Pt-adsorbed catalyst, the energy profiles of various reaction intermediates were calculated on this model. A catalytic cycle constituted FA adsorption, C—O bond scission, with H back donation from the leaving -OH to C, followed by 2MF desorption, was finally drawn. At 0.04% loading, Pt atoms were highly active and when the loading was increased to 1%, they tended to aggregate to form nanoparticles. Extended in-situ x-ray absorption fine structure

(EXAFS) spectras of 1% Pt nanoparticle-loaded TiO_2 show a sharp peak at 1.86 Å due to the bond between Pt atoms and the TiO_2 matched with α-PtO_2 (Pt−O bond $-> 1.86$ Å, the nearest Pt, and the second-shell O − 2.7 and 3.3 Å). A weak peak around 2.3 Å was observed due to the Pt-Pt bond (2.3 Å and 2.9 Å) as present in Pt metal. For the lowest Pt loaded TiO_2 (0.04%Pt-TiO_2) sample, the peaks due to the first-shell Pt−Pt contribution and the second-shell Pt−O contribution being absent, that validates the absence of Pt nanoparticles. Further, x-ray absorption near edge structure (XANES) and x-ray photoelectron spectroscopy (XPS) spectra confirm that Pt was cationic and remains oxidized even at elevated temperature. Further, Fourier transform infrared (FTIR) spectrum of 1% Pt/TiO_2 showed a broad peak from 2060 to 2089 cm^{-1}, assigned to CO adsorbed on well-coordinated ($\sim$2080 cm^{-1}) and undercoordinated (2,060 cm^{-1}) Pt^0 metal sites. As the Pt loading was decreased to 0.04%, a new peak at 2118 cm^{-1} could be assigned to CO adsorbed on isolated $Pt^{\delta+}$ atoms, suggesting the presence of isolated Pt atoms. To probe the synergistic role of atomic Pt and TiO_2 in HDO reaction, pristine TiO_2 and silica-supported Pt nanoparticles (0.1% Pt/SiO_2) were tested for the HDO of FA. As expected, pure TiO_2 displayed low HDO activity without affecting the ring chemistry while 0.1% Pt/SiO_2 showed nonselective HDO with FA ring hydrogenation. When 0.04% Pt/TiO_2 is used as catalyst, no ring chemistry was observed and the HDO rate was increased 31-fold in comparison to pristine TiO_2 ascribed to an increased number of oxygen vacancies in the vicinity of Pt. Highly dispersed Pt stabilized on TiO_2 hampers the ring chemistry due to the ensemble effect. Furthermore, adsorption of 2,5-dimethylfuran (DMF) was weak on the atomically dispersed catalyst, and the bond length of the furan ring remains the same as those in gaseous DMF (Fig. 4−4).

4.3.2 Cellulose to ethylene glycol and acetol conversion

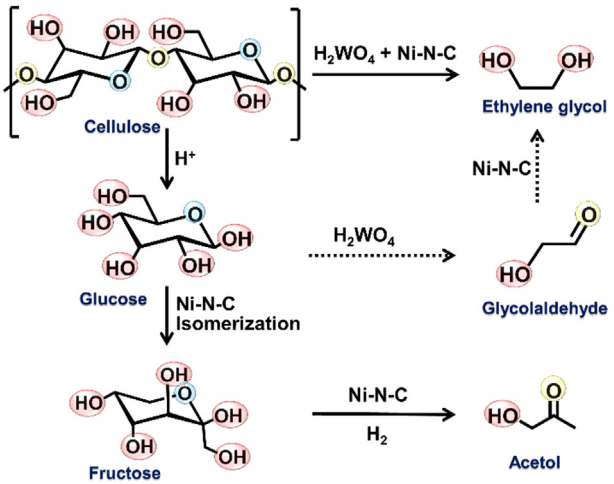

Nickel catalysts are widely used for activated hydrogen-assisted biomass conversions such as hydrogenation, hydrogenolysis, and hydrodeoxygenation reactions due to its inexpensive,

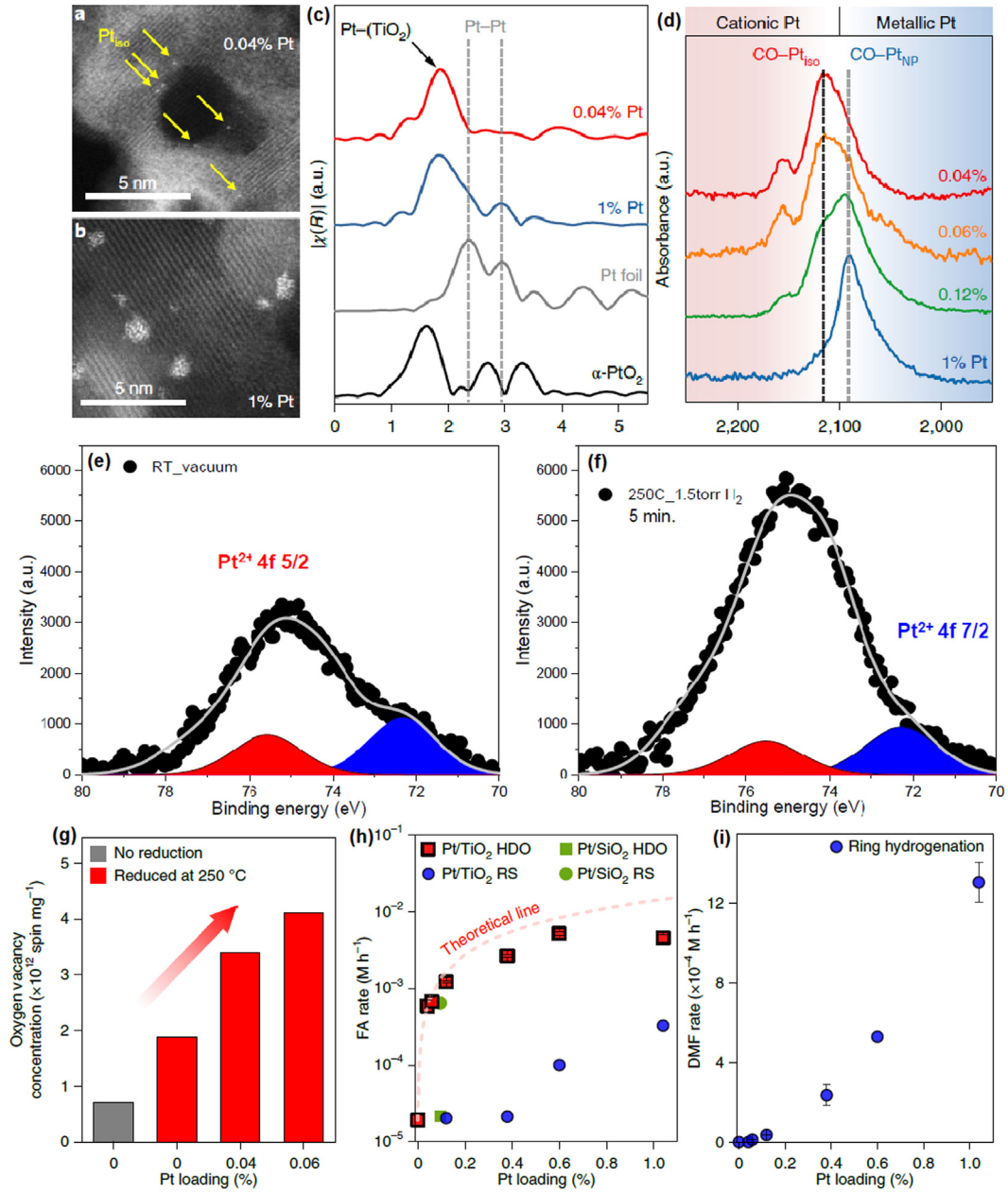

FIGURE 4–4 (a) HADDF-STEM images of 0.04% Pt/TiO_2, and (b) 1% Pt/TiO_2 catalysts after reduction. Arrows mark isolated Pt atoms (Pt_{iso}); (c) The k^2-weighted EXAFS spectra of Pt/TiO_2 catalysts and Pt standards at the Pt L_3 edge. $\chi(R)$ denotes the magnitude of the Fourier-transformed EXAFS spectra. Identical parameters are used for background removal and forward Fourier transform: the frequency cut-off parameter $R_{bkg} = 1.1$ Å, k range $\Delta k = 2-10$ Å^{-1}. The dashed lines indicate peaks corresponding to the Pt−Pt first coordination shell, (d) FTIR-CO spectra of Pt/TiO_2. The dashed line on left indicates the position of the peak assigned to CO adsorbed on isolated

earth abundance, and excellent activity [90–92]. Unfortunately, their susceptibility to agglomerate, leach out and deactivation via dissolution under acidic conditions, restricts their application. The encapsulation of Ni in porous supports and alloy formation with other metals is envisaged to solve the problem, but it compromises activity due to mass transfer limitations [93,94]. SACs with a composition M–N–C (M metals such as Fe, Co, Ni) containing a metal center coordinated with N core-bonded with carbon skeleton has been proven an excellent acid and heat resistant catalyst [95–97]. Achieving high metal loading for Ni–N–C SACs is highly desirable to get practical hydrogenation rates for the application in biomass valorization. A Ni–N–C SAC with a high Ni content c.a. 7.5 wt.% (ICP) was prepared by pyrolysis of a $Ni(phen)_3$ complex dispersed on MgO at 600°C in N_2 for 2 h followed by etching of MgO supports [98]. Among catalysts prepared at 500, 600, and 700°C, the Ni–N–C–600°C shows the highest surface area reaching up to 500 $m^2 g^{-1}$ while for Ni–N–C–700 the surface area was decreased due to structural collapse of nanoparticles formation. XANES spectra of the three Ni–N–C SACs show distinct features. The order of E_0 value for the oxidation state was found Ni foil < Ni–N–C–700 < $Ni^{II}Pc$ < Ni–N–C–600 < Ni–N–C–500 < Ni_2O_3, suggesting the oxidation state of Ni single-atoms is between Ni^{II} and Ni^{III}. The XANES spectrum of the Ni–N–C–600 catalyst displayed four distinct peaks A, B, C, and D at 8333 (pre-edge), 8339 (pre-edge), 8351 (absorption-edge) and 8366 eV (post-edge). The pre-edge peaks at 8333 and 8339 eV were assigned to 1 s→3d, 1 s→$4p_z$ electronic transition suggesting: (1) Ni cations are in a distorted octahedral geometry originating from slight (p-d) orbital mixing, and (2) square-planar M-N4 moiety in a distorted state as compared to $Ni^{II}Pc$ [99,100]. The absorption edge peak C was corroborated to transition from 1 s to 4p continuum states while peak D was originated from the multiple scattering. Density functional theory (DFT) calculations on various models were run; the corresponding XANES spectrum calculated show only (Ni–N4)···N configuration perfectly matched with the experimental spectrum of Ni–N–C–600 catalyst. In this model, four pyridinic N atoms were coordinated with the central Ni to form a distorted quasi-planar Ni-N4 structure and the fifth pyridinic N atom weakly coordinated to the Ni atom in the perpendicular direction, suggesting distorted octahedral coordination geometry Ni-N5 structure with a ligand missing. XPS spectra also show a 4.4:1 ratio between pyridinic N and Ni that was in close agreement with XANES optimized Ni-N5 structure, validating a homogeneously distributed structure throughout the catalyst. EXAFS results at the Ni K-edge showing a peak at 1.40 Å, similar to the feature of $Ni^{II}Pc$ and after the EXAFS fitting exhibited two distinct Ni-N coordination shells, with a 3.4 and 1.7

◀ Pt atoms, whereas the yline on right indicates a peak maximum at 2,089 cm^{-1} for CO on 1% Pt/TiO_2.; (e) deconvoluted Pt4f, Cu3p in situ XPS spectra of 0.04% Pt/TiO_2 measured at room temperature and vacuum; and (f) 1.5 Torr H_2, and promotional effects of Pt dopant on oxygen vacancy formation and selective C–O bond scission; (g) quantitative EPR analysis at room temperature; (h) HDO and ring saturation (RS) rates over Pt/TiO_2 (squares and circles with boundry, respectively) and Pt/SiO_2 (square and circle without boundry). The RS rate is below detection for ≤0.06% Pt/TiO_2. (i) DMF hydrogenation rate at various Pt loadings. Reaction conditions: 0.088 M FA (or DMF), 20 mL 2-propanol, 100 mg catalyst, reaction temperature at 160°C, 100 psi H_2, and 160 psi N_2 measured at room temperature [89]. *Reproduced with permission from J. Fu, J. Lym, W. Zheng, K. Alexopoulos, A.V. Mironenko, N. Li, et al., C–O bond activation using ultralow loading of noble metal catalysts on moderately reducible oxides, Nat. Catal., 3 (2020) 446–453. Copyright 2020 Nature Publishing Group.*

coordination that matched well with XANES and DFT results. The reported catalyst demonstrated excellent reduction performance for a wide variety of unsaturated functional groups present in the biomass such as nitroarenes (−NO_2), aldehyde (−C═O), styrene (−C═C−), phenylacetylene (−C≡C−), and quinoline (−C═N−). The control experiment using pyrrole as a Lewis acid and SCN^- ions as Ni cations poison (Lewis acid sites) showed a remarkable drop in activity, confirming Ni cations (Lewis acid sites) and the neighboring non-coordinated pyridinic N atoms (Lewis basic sites) work as a frustrated Lewis pair. Additionally, the actual hydrolysis of cellulose using Ni−N−C−600 and tungstic acid (promotes C−C cleavage via a retro-aldol pathway) under harsh reaction condition (245 °C, 60 bar H_2, strongly acidic hydrothermal conditions) yielded EG (36.8%) and acetol (17.4%) as main products (other products: hydroxyacetone, glycerol, isosorbitol, mannitol, 1,2-butanediol, erythritol 1,2-propylene glycol, etc.) without deactivation of the catalyst. The catalyst showed a negligible reduction in activity after several reaction cycles and had identical atomic distribution as in fresh catalyst (Fig. 4−5).

4.3.3 Hydrogenation of furfural to furfuryl alcohol

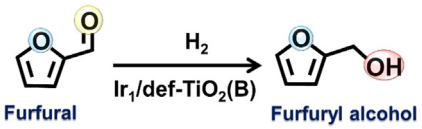

Furfural is an important biomass feedstock that can be used to produce a wide variety of chemicals [101,102]. The selective chemical hydrogenation of furfural to furfuryl alcohol is an important step to produce fine industry chemicals and biofuels. Current processes for hydrogenation of furfural to furfuryl alcohol rely on the toxic chromium-based catalyst and require harsh reaction conditions [103]. Noble metals are excellent hydrogenation catalysts, however, due to poor selectivity, side products such as tetrahydrofurfural, tetrahydrofurfuryl alcohol, furan, tetrahydrofuran, or levulinic acid are produced in large quantities [104−106]. SACs of noble metals have the potential to selectively reduce furfural to furfuryl alcohol and alleviate the use of toxic chemicals. To check the performance for hydrogenation of furfural to furfuryl alcohol on SACs, iridium single-atom catalysts were made on defective phase titanium dioxide nanosheets (Ir_1/def-TiO_2(B)) and mesoporous graphitic carbon nitride (Ir_1/mpg-C_3N_4) [107]. It was found that the as-prepared Ir_1/def-TiO_2(B) catalyst exhibited outstanding conversion (99%), high selectivity (99%), and good stability in the hydrogenation of furfural to furfuryl alcohol, which is superior to Ir_1/mpg-C_3N_4 and the Ir nanoparticles. The increased peak intensity of def-TiO_2(B) in the Ti K-region of XANES spectra and presence of EPR signals at a g-value of 2.003 in comparison to nondefected per-TiO_2(B) suggest the presence of oxygen point defects. The TEM and HAADF-STEM images of 0.10 wt.% Ir-containing catalyst did not show the presence of any nanoparticles. Aberration-corrected HAADF-STEM which differentiates the high atomic number Ir from Ti and O due to Z-contrast showed many small

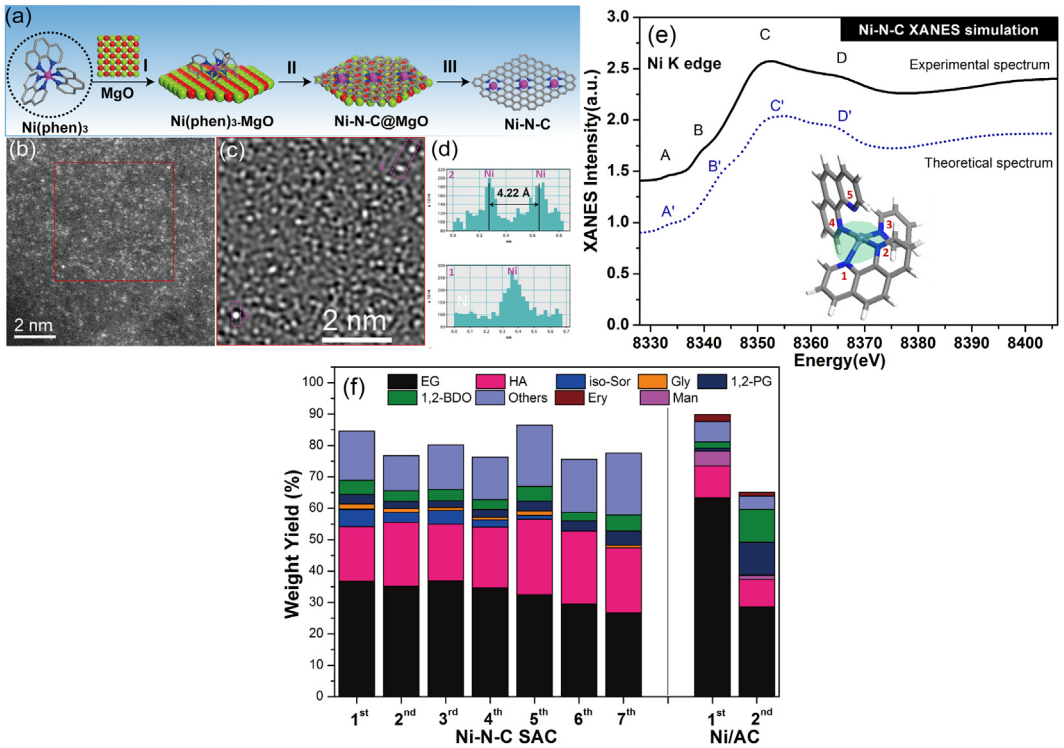

FIGURE 4–5 (a) Synthetic scheme of the Ni-N-C catalyst; (b) HAADF-STEM image; (c) fast Fourier transform (FFT image); (d) intensity profiles along the lines at positions 1 and 2 in the HAADF-STEM image; (e) comparison of experimental and calculated XANES spectra of the Ni—N—C—600, and the inset shows the structure model of Ni-N5; and (f) the durability of the Ni—N—C—600 in comparison with Ni/AC for the one-pot conversion of cellulose. Reaction conditions: 0.3 g cellulose, 50 mg catalyst, 30 mg tungstic acid, and 30 mL water in 100 mL autoclave, 245 °C, 6.0 MPa H_2, 1 h 45 min, 1000 rpm. Product Code: EG: ethylene glycol; HA: hydroxyacetone; iso-Sor: isosorbitol; Man: mannitol; Gly: glycerol; 1,2-PG: 1,2-propylene glycol; 1,2-BDO: 1,2-butanediol; Ery: erythritol and others [98]. *Reproduced with permission from W. Liu, Y. Chen, H. Qi, L. Zhang, W. Yan, X. Liu, et al., A durable nickel single-atom catalyst for hydrogenation reactions and cellulose valorization under harsh conditions, Angew. Chem., 130 (2018) 7189—7193. Copyright 2018 Wiley-VCH.*

bright dots, validating the homogeneous distribution of Ir on the def-TiO_2(B). The Ir *L3*-edge XANES spectra and XPS spectra of the Ir_1/def-TiO_2(B) and the Ir_1/mpg-C_3N_4 catalyst reveals oxidized Ir_1 species with a different positive charge for def-TiO_2(B) and mpg-C_3N_4 support. The presence of peak due to Ir − O shell (R ∼ 1.7 Å) and the absence of Ir-Ir peak in EXAFS spectra further confirm atomically distributed Ir in an oxidized state. The first principle calculation demonstrates four types of oxygen vacancies among which (010) surface configuration in which the Ir atom is bonded to three Ti atoms is energetically most favorable.

Further, the adsorption energies of furfural on Ir_1/mpg-C_3N_4, Ir_1/def-TiO_2(B), and Ir_{147} nanoparticle were found to be 0.60, 1.63, and 3.41 eV respectively, suggesting furfural bound very weakly to Ir_1/mpg-C_3N_4 while very strongly to Ir_{147} nanoparticles. The moderate bonding of furfural with the Ir_1/def-TiO_2(B) sample was caused by the interaction of furfural

molecules with Ir single-atom and an adjacent Ti atom, which increases the adsorption energy resulting in the best catalytic performance. In contrast, furfural adsorbs on Ir_1/mpg-C_3N_4 with an Ir single-atom and no neighboring atoms participate in bonding, resulting in the weak interaction. Similarly, for the Ir_{147} nanoparticles, a strong chemical interaction of furfural with four Ir atoms resulted in the strongest interaction and least desorbed product. An energy coordinate of furfural to FA was calculated that proceeds through adsorption of furfural and H_2 to formaldehyde and a successive reduction to alcohol. The recycling experiment shows that Ir_1/def-TiO_2(B) catalyst remains equally active as a fresh catalyst and shows atomic dispersion even after five runs, demonstrating the stability of the catalyst (Fig. 4–6).

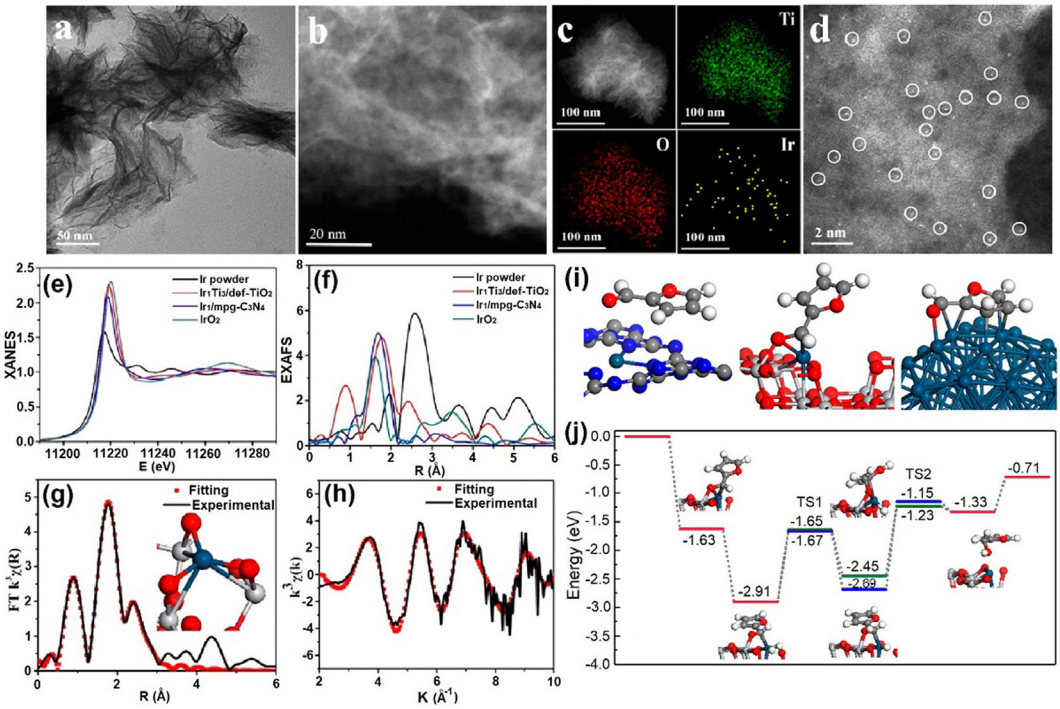

FIGURE 4–6 (a) TEM image and (b) HAADF-STEM image of an Ir_1/def-TiO_2(B) nanosheet; (c) EDX elemental mapping analysis for the distributions of Ti, O, and Ir; (d) AC HAADF-STEM image of the Ir_1/def-TiO_2(B) sample and X-ray absorption analysis; (e) XANES spectra at the Ir L_3- edge of the Ir power, Ir_1/def-TiO_2(B), Ir_1/mpg-C_3N_4, and the IrO_2 samples; and (f) Fourier transform (FT) at the Ir L_3-edge of the above four materials. (g) and (h) Corresponding fits of the EXAFS spectrum of Ir_1/def-TiO_2(B) at the R space and the k space, respectively, (solid line: experimental data; dots: fitting data). The inset of panel (g) shows the local structure of the Ir_1 species on def-TiO_2(B) obtained from the DFT simulations; (i) Adsorption configurations of a furfural molecule on the Ir_1/ mpg-C_3N_4 monolayer (left), the Ir_1/def-TiO_2(B) substrate (middle), and the Ir_{147} nanoparticle (right); and (j) Energy profile (unit: eV) and reaction pathway for the catalytic hydrogenation of furfural to furfuryl alcohol at the Ir_1 active site on def-TiO_2(B). Structures of all the intermediate states are also shown on the energy profile [107]. *Reproduced with permission from S. Tian, W. Gong, W. Chen, N. Lin, Y. Zhu, Q. Feng, et al., Regulating the catalytic performance of single-atomic-site Ir catalyst for biomass conversion by metal–support interactions, ACS Catal., 9 (2019) 5223–5230. Copyright 2019 American Chemical Society.*

4.3.4 Hydrogenation of levulinic acid to γ-valerolactone

The valorization of cellulosic biomass also produces levulinic acid (LA) which serves as an important precursor for green solvents (γ-valerolactone), plasticizers, biofuel, pharmaceutical, cosmetics (ethyl levulinate), biodegradable herbicides (aminolevulinic acid), fuel and additives (2-methyl-THF), etc [109−112]. Hydrogenation of levulinic acid (LA) to γ-valerolactone (GVL) is of utmost importance as GVL is the platform molecule used in many of those upgrading routes [113−115]. Existing biomass valorization techniques operate in the liquid phase under harsh reaction conditions such as high temperature and pressure, and use corrosive acidic reaction media. Noble metals catalysts such as Ru, Pt, Ir, Pd, etc., supported on an inert substrate such as activated carbon, has shown great promise for hydrogenation of LA to GVL, but leaching from the substrate, cessation of catalytic activity in acidic conditions, and nonselective hydrogenation leading to by-product formations are major issues [116−118]. Ir-based catalysts, especially homogeneous metal complexes such as polyazines, and pincer complexes, can reach up to 99% conversion efficiency with good selectivity, but their difficult and tedious separation makes them inapplicable [119,120].

To overcome these problems, Cao et al. synthesized an ultra-stable 0.6 wt.% Ir@ZrO_2@C SAC via an in-situ grafting of Ir metal during assembly of UiO-66 MOF, followed by confined pyrolysis [108]. The XPS spectra of 0.6 wt.% Ir@ZrO_2@C SAC showed a single peak due to $Ir^{\delta+}$ from an isolated atomically dispersed Ir coordinated with the ZrO_2 matrix while Ir/C and Ir/ZrO_2 reveals Ir^0, $Ir^{\delta+}$, and Ir^{4+} peaks due to the presence of metallic Ir, isolated Ir single-atoms, and IrO_x/IrO_2 species. The H_2-TPR analysis shows only one reduction peak for Ir@ZrO_2@C SAC at a relatively higher temperature (182°C) compared to Ir/C nanocatalyst and Ir/ZrO_2 which shows Ir oxide reduction peaks around 82°C. This confirms the presence of only single-atom sites in the catalyst. The synthesized Ir@ZrO_2@C SAC displayed excellent stability in the selective hydrogenation of LA to GVL without a sign of deactivation even after six and seven consecutive runs at pH = 3 and one respectively at 180°C and 40 bar H_2. The performance of SAC was compared with standard 2.7 wt.% Ir/C and 0.6 wt.% Ir/ZrO_2 nanocatalysts, which showed significant deactivation and leaching under the same conditions. The 2.7 wt.% Ir/C catalyst show 5.8% leaching after the first recycle while 0.6 wt.% Ir/ZrO_2 catalyst show 6.7% leaching and a GVL yield drop from ∼ 56% to 43% after three runs with pH-3. The STEM, EDX mapping, and AC-HAADF-STEM measurements of 0.6 wt.% Ir@ZrO_2@C SAC show atomic dispersion of Ir and no aggregation even after seven reuses. The LA to GVL conversion yield of Ir/C and Ir/ZrO_2 was 95% in 20 min and 98% in 80 min corresponded to 0.67 s^{-1} and 0.32 s^{-1}, turn over frequency (TOF). The obtained GVL yield of Ir@ZrO_2@C SAC was much lower (98.8% after 10 h; TOF of 0.034 s^{-1}), however, an astonishing > 99% selectivity without a trace of any by-product.(Fig. 4−7)

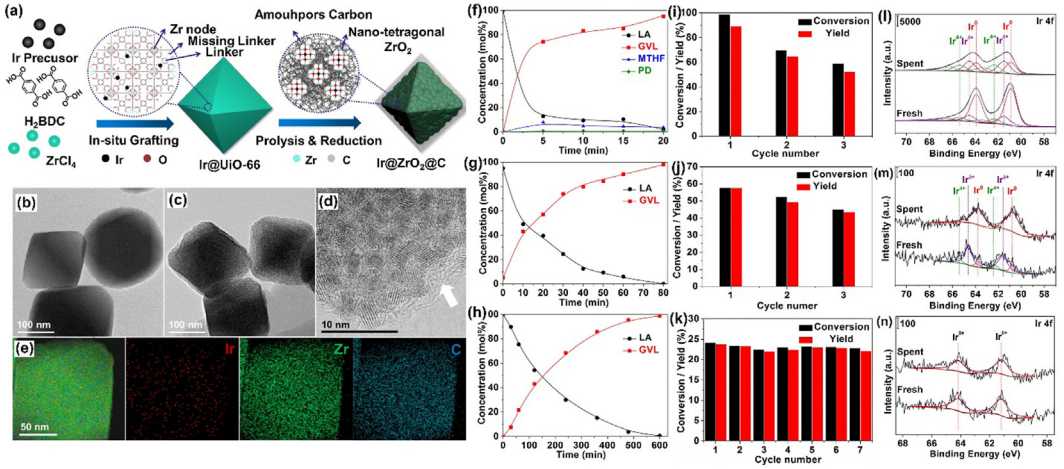

FIGURE 4–7 (a) Schematic illustration of the in-situ synthesis approach for the synthesis of 0.6 wt.% Ir@ZrO_2@C, STEM images of (b) Ir@UiO-66, (c) 0.6 wt.% Ir@ZrO_2@C, (d) high-resolution STEM image and (e) EDX-mapping analysis of the 0.6 wt.% Ir@ZrO_2@C. Time profiles of catalytic conversion of 10 wt.% levulinic acid in water using (f) 2.7 wt.% Ir/C, (g) 0.6 wt.% Ir/ZrO_2, and (h) 0.6 wt.% Ir@ZrO_2@C as the catalysts. The recycling experiments of (i) 2.7 wt.% Ir/C (10 min), (j) 0.6 wt.% Ir/ZrO_2 (20 min), and (k) 0.6 wt.% Ir@ZrO_2@C (1 h) in a pH = 3 aqueous solution. Ir 4 f XPS of the (l) fresh and spent (three-times recycled) 2.7 wt.% Ir/C nanocatalyst in a pH = 3 aqueous solution; (m) fresh and spent (three-times recycled) 0.6 wt.% Ir/ZrO_2 nanocatalyst in a pH = 3 aqueous solution; and (n) fresh and spent (seven times recycled) 0.6 wt.% Ir@ZrO_2@C SAC in a pH = 3 aqueous solution [108]. *Reproduced with permission from W. Cao, L. Lin, H. Qi, Q. He, Z. Wu, A. Wang, et al., In-situ synthesis of single-atom Ir by utilizing metal-organic frameworks: An acid-resistant catalyst for hydrogenation of levulinic acid to γ-valerolactone, J. Catal., 373 (2019) 161–172. Copyright 2019 Elsevier.*

4.3.5 Oxidation of 5-hydroxymethylfurfural to 2,5-diformylfuran

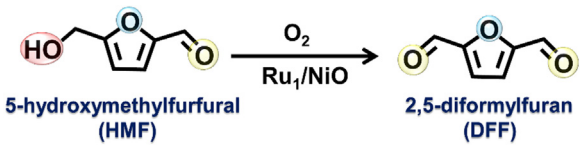

5-Hydroxymethylfurfural (HMF) is another platform molecule derived from the acid-assisted valorization of biomass [121]. HMF can be oxidized to 2,5-diformylfuran (DFF) which is an interesting substrate to produce biopolymers, drugs, antifungal, macrocyclic ligands, etc [122,123]. The transformation of HMF to DFF is a challenging reaction from the chemistry point of view because it requires controlled oxidation of primary alcohol while leaving the aldehyde group intact. Many stoichiometric/nonstoichiometric catalytic systems such as pyridinium chlorochromate, $K_2Cr_2O_7$–dimethylsulfoxide, 2,2,6,6-tetramethylpiperidine-1-oxide (TEMPO), H_2O_2 and sodium hypochlorite, have been reported for the oxidation of HMF to DFF, but they afford poor yield and unselective oxidation [124,125]. Supported noble-metal nanoparticle catalysts, specifically the Ru-based catalyst, have shown good performance for

catalytic oxidation of HMF into DFF [122,126]. Ru-based SACs can further improve the performance and selectivity of the reaction due to the ensemble effect (the combined synchronized effect of groups/metal/compounds ameliorating the performance of catalyst than individual components). Recently, Liu et al. used ball milling as a facile, low-cost synthetic strategy for Ru single-atoms supported on NiO (Ru_1/NiO) catalyst using ruthenium(III)-2,4-pentanedionate and nickel(II) acetylacetonate (1:400) precursor followed by calcination at 400°C [124]. The characterization of Ru_1/NiO using TEM, STEM, and AC-HAADF shows the atomic distribution of the Ru on the NiO surface. The absence of any Ru nanoparticle peak in XRD and Ru3d XPS peak due to $+2$ and $+3$ state confirm atomically distributed Ru cation in NiO lattice. Additionally, 0.14 wt.% Pt_1/NiO and 0.29 wt.% Pd_1/NiO SACs were also prepared and tested for the oxidation of HMF into DFF. The Ru_1/NiO SAC demonstrated the highest conversion (91.1%) while selectivity reached up to 81.3% higher compared to Pt_1/NiO (31.6%) and Pd_1/NiO (38.4%). Changing the support from NiO to ZnO and FeO_x in 0.23 wt.% Ru_1/ZnO, and 0.26 wt.% Ru_1/FeO_x detrimentally reduced the conversion up to 40.6% and 48.4%, respectively, suggesting a synergistic interaction between NiO and Ru was key for improved performance. The Ru_1/NiO SAC shows almost unchanged activity after three recycle runs; AC HAADF-STEM and XPS showed no change in the morphological and chemical state (Fig. 4−8).

4.3.6 Selective hydrogenolysis of glycerol to 1,2-propanediol or propylene glycol

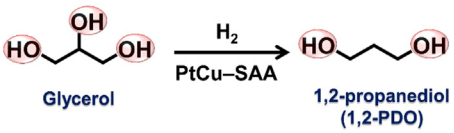

Another important biomass-derived platform chemical is glycerol which is the smallest representative of polyols. Glycerol is produced as a by-product during biodiesel production from the transesterification of vegetable oils (triglycerides) and methanol [127,128]. A fraction of glycerol is also produced as a by-product of bioethanol production from lignocellulose [129]. The production of glycerol during biodiesel production is 10% w/w of the actual product means for every 9 kg of biodiesel, 1 kilogram of crude glycerol is produced (Pachauri, 2006) [130]. Since biodiesel production has skyrocketed in the past few years, the price of glycerol has dropped significantly. Except for some limited applications such as food, cosmetic, coolant, and polymer industries, the glycerol has limited commercial utility. So it is imperative to use glycerol for the production of value-added chemicals [19,131].

Various strategies have been proposed for the conversion of glycerol into commodity chemicals, such as oxidation (oxalic acid, glyceraldehyde, etc), hydrogenolysis (1,2 propanediol, 1,3 propanediol, ethylene glycol), dehydration (acrolein), selective esterification (monoglycerides and glycerol dimethacrylate), and carboxylation (glycerol carbonates) [132−139].

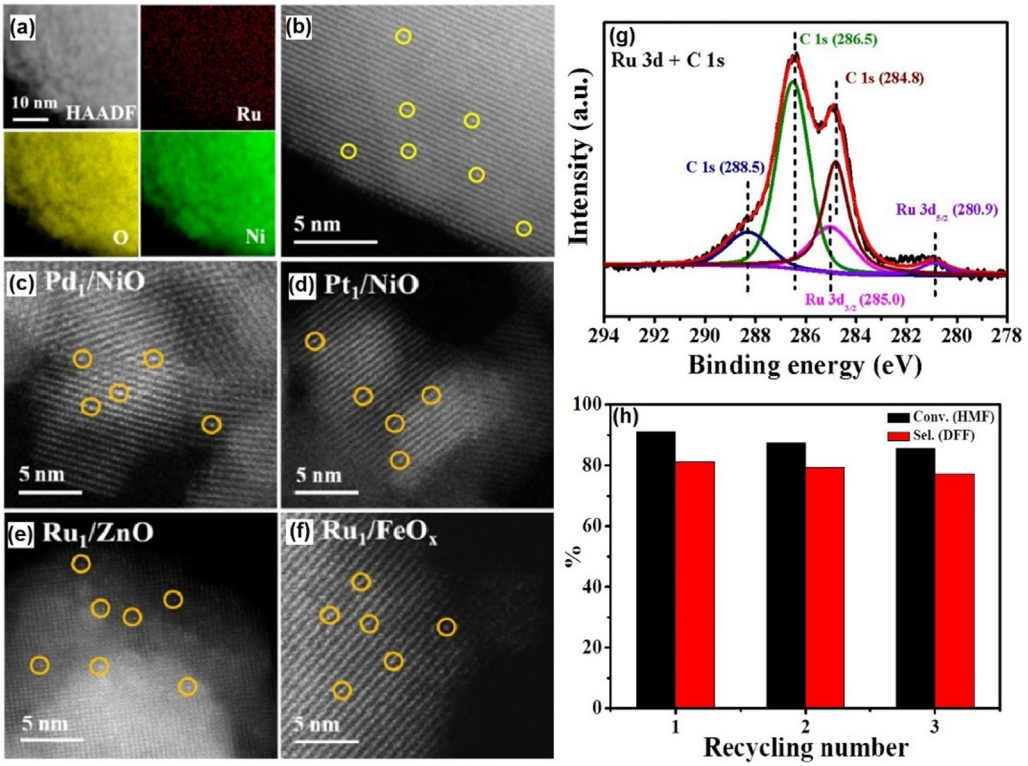

FIGURE 4–8 (a) Elemental mapping images Ru_1/NiO and AC HAADF-STEM image of (b) Ru_1/NiO. (c) Pd_1/NiO, (d) Pt_1/NiO, (e) Ru_1/ZnO, and (f) Ru_1/FeO_x, (g) Ru3d XPS spectrum of Ru_1/NiO and (h) Catalyst recycling experiments for Ru_1/NiO [124]. *Reproduced with permission from Y. Liu, T. Gan, Q. He, H. Zhang, X. He, H. Ji, Catalytic oxidation of 5-hydroxymethylfurfural to 2, 5-diformylfuran over atomically dispersed ruthenium catalysts, Ind. Eng. Chem. Res., 59 (2020) 4333–4337. Copyright 2020 American Chemical Society.*

Some other approaches are pyrolysis to produce syn-gas and microorganisms assisted conversion to citric acid, 1,3 propanediol, poly(hydroxyalkanoates) (PHA), etc [140,141]. Among all these processes selective hydrogenolysis of glycerol to 1,2-propanediol (1,2-PDO) or propylene glycol is attractive because of its usage in the synthesis of wide varieties of commodity chemicals such as unsaturated polyester resin, food additives, antifreeze, and cosmetics. The main challenge associated with the transformation of glycerol to 1,2-PDO is selective cleavage of terminal C—O bond without breaking another C—O/C—C bond of the carbon chain. Alloyed catalyst has shown great promise over single component noble metal (Pd, Ru, and Pt, etc.) or nonnoble metal catalysts (Cu, Ni, and Co) catalyst due to synergistic interaction [137,142–146]. The performance of bimetallic catalysts can be further maximized by dispersing a single-atom on another active metal to form a single-atom alloy (SAA) catalyst, utilizing each atom in the surface of the catalyst. The Cu-based catalyst shows high selectivity toward C—O bond cleavage without scissoring C—C bond, but deactivation at high temperatures and poor activity are limiting parameters [147]. On the other hand, Pt-based catalysts are

extremely active but have less selectivity for C—O bond cleavage [148]. So for taking advantage of the high selectivity of Cu and high activity of Pt, Zhang et al. prepared a PtCu single-atom alloy (SAA) catalyst by decorating a single Pt atom on Cu nanoclusters using a hydrotalcite layered double hydroxide (CuMgAl—LDH) precursor and sequential oxidation at 500°C to form mixed metal oxides (MMO); the reduction under H_2 followed by a galvanic replacement reaction [149]. The developed PtCu—SAA exhibited excellent catalytic performance reaching a 99.6% conversion and 99.2% selectivity with a turnover frequency (TOF) of up to 2.6×10^3 $mol_{glycerol} \cdot mol_{PtCu-SAA}{}^{-1} \cdot h^{-1}$ for hydrogenolysis of glycerol to 1,2-propanediol under mild reaction conditions (200°C, 2 MPa). HR-TEM images show crystal planes of Cu(111) while aberration-correction high-angle annular dark-field scanning transmission electron microscopy (AC—HAADF—STEM) imaging confirmed the atomic distribution of Pt atoms surrounded by Cu atoms. In situ CO—DRIFTS (diffuse reflectance infrared Fourier transform spectroscopy) experiment on PtCu—NPs and Pt/ MMO samples shows two bands at 2010—2060 and 1810—1880 cm^{-1} due to linear and bridged carbonyl between two adjacent Pt atoms. PtCu—SAA catalyst shows a broad absorption band in between 2060 and 2140 cm^{-1} which after deconvolution gave two peaks at 2097 cm^{-1} and 2116 cm^{-1} due to CO chemisorbed on Cu^0 and Cu^+ species, while the third peak centered at 2088 cm^{-1} was corroborated to isolated single Pt atoms linearly bounded to CO. EXAFS of PtCu—SAA at the Pt-*L3* edge displayed a single peak at ~2.2—2.3 Å centered between PtO_2 and Pt peaks, due to different coordination environment of Pt in SAA. The coordination of PtCu—SAA sample was found to be ~7.4 Pt—Cu that did not match with Pt—Pt or Pt—O coordination, validating an isolated single Pt atom was surrounded by Cu atoms. In comparison to Pt/MMO which displays no peak and Cu/MMO which displays a sharp intense peak at 146°C, the PtCu—SAA sample shows an asymmetrical peak around 106°C in H_2-TPD, suggesting atomically distributed Pt enhances hydrogen dissociation and spillover capacity. In situ XANES spectra of PtCu—SAA at Cu—K edge and Pt-*L3* edge show that after the addition of glycerol to fresh catalyst, a fraction of Cu^0 gets converted to Cu^+ while Pt was transformed into a low oxidation state. Based on in situ glycerol-DRIFTS measurement, it was found that, for Pt/MMO and Cu/MMO catalysts, dehydrogenation proceeds with glyceraldehyde as an intermediate and for PtCu—SAA acetol (Pt—Cu) and glyceraldehyde (Cu—Cu) were the intermediates (Fig. 4—9).

4.3.7 Temperature controlled selective transformation of vanillin to vanillyl alcohol and 2-methoxy-4-methylphenol

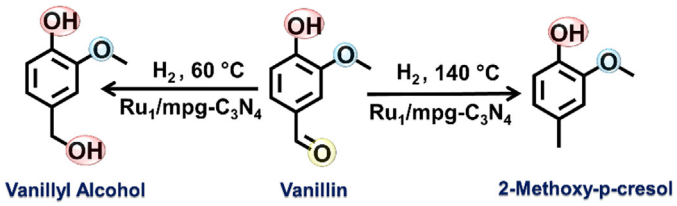

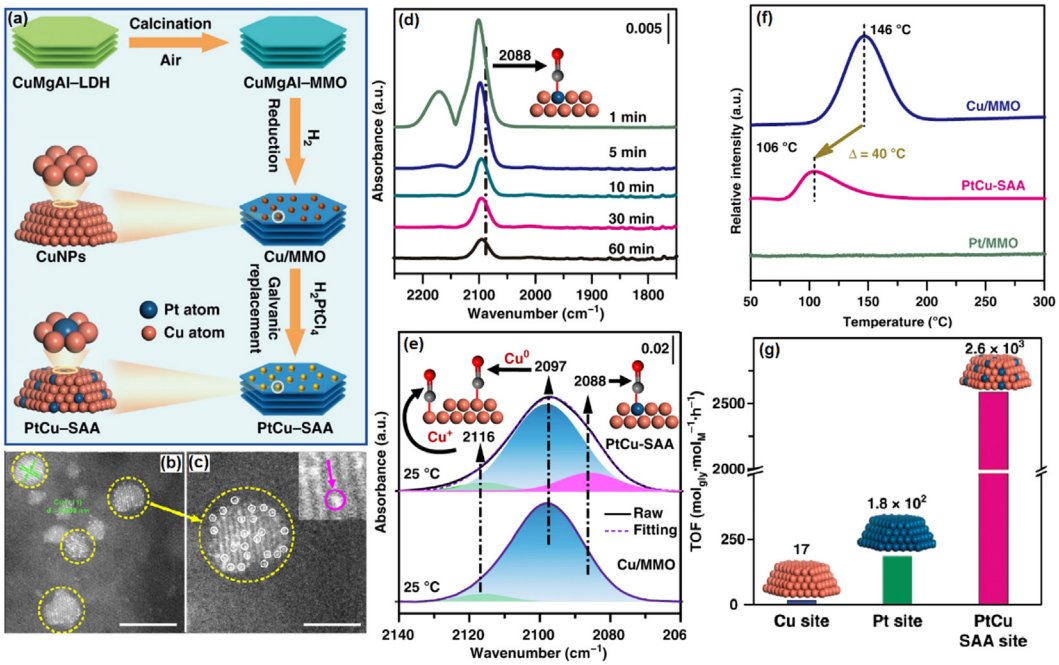

FIGURE 4–9 (a) A schematic illustration for the preparation of PtCu−SAA, (b) AC−HAADF−STEM image of PtCu−SAA, (c) corresponding enlarged images at 2 nm scale bar, (d) In situ CO-DRIFTS spectra of PtCu−SAA, and (e) in situ CO-DRIFTS spectra of Cu/MMO and PtCu−SAA at 25°C (solid line: experimental data; dotted line: fitting curve). (f) Surface H_2−TPR spectra of various samples after N_2O−oxidation pretreatment: Pt/MMO, PtCu−SAA, and Cu/MMO. (g) Catalytic evaluation of PtCu-SAA and monometallic catalysts (Pt/MMO and Cu/MMO) toward glycerol hydrogenolysis to 1,2-PDO; the TOF value determined as moles of initial glycerol converted per mole of exposed active sites per hour in the catalytic dynamic range. [149] *Reproduced with permission from X. Zhang, G. Cui, H. Feng, L. Chen, H. Wang, B. Wang, et al., Platinum−copper single-atom alloy catalysts with high performance towards glycerol hydrogenolysis, Nat. Commun., 10 (2019) 5812. Copyright 2019 Nature Publishing Group.*

Lignin is a main component of biomass, comprised of cross-linked phenolic polymers and about 30% of wood waste. This lignin-based waste can be pyrolyzed followed by hydrogenation to get biofuel. Vanillin (4-Hydroxy-3-methoxybenzaldehyde) is a common component of lignin pyrolysis oil which can be hydrogenated/hydro-deoxygenated (HDO) to vanillyl alcohol and 2-methoxy-4-methylphenol, a potential future biofuel [150−153]. The hydrogenation of carbonyl groups into hydroxyl groups is easy. However, selective reduction of the hydroxyl group via deoxygenation to get alkyl derivative is the main challenge. The selective hydrodeoxygenation of these phenolic components will play an important role in upgrading biofuel and the production of value-added products. Tian et al. synthesized mesoporous carbon nitride, supporting a isolated single-atom Ru catalyst (Ru_1/mpg-C_3N_4) by a simple wet impregnation method [154]. The absence of any XRD peak for Ru NPs, HAADF-STEM, and EDX mapping confirms the atomic distribution of Ru in mesoporous structure.

The Ru content was found to be at 0.10 wt.% as determined from inductively coupled plasma optical emission spectrometry (ICP-OES). Ru K-edge XANES spectra of Ru_1/mpg-C_3N_4 show an absorption edge of single-atom Ru in between Ru and RuO_2, due to partly positive Ru interacting with C_3N_4 support. The presence of a single peak in Fourier transformed (FT) k3-weighted EXAFS of Ru_1/mpg-C_3N_4 due to Ru−N contribution, and absence of any peak at ∼2.6 Å due Ru−Ru contribution, validate the presence of a single-atom in the matrix. The developed material demonstrated excellent conversion and selectivity for the hydrogenation and hydro-deoxygenation of vanillin to vanillyl alcohol and 2-methoxy-*p*-cresol or methoxyphenol. Interestingly, hydrogenation of vanillin into vanillyl alcohol at 60°C showed ∼100% selectivity and 95% conversion. At 120°C a mixture of vanillyl alcohol and 2-methoxy-*p*-cresol was obtained and further increase in temperature at 140°C only 2-methoxy-*p*-cresol was observed with ∼100% conversion and selectivity. The first principle calculation was used for investigating the reason for this unprecedented selectivity at different temperatures. Among four possible optimized structures of Ru_1/mpg-C_3N_4, the structure where Ru coordinated with three N atoms and one C atom show the highest adsorption energy for vanillin and H_2. The reaction proceeds with adsorption of vanillin on the Ru site, and the free energy of adsorption was obtained −0.42 eV and −0.21 eV at 60°C and 140°C, respectively. The energetics of the intermediate state clearly show that hydrogenated 2-methoxy-*p*-cresol is thermodynamically more stable than the partially hydrogenated vanillyl alcohol and the high energy of IM2 hydrogenation makes vanillyl alcohol as deoxygenation prohibited product and 2-methoxyl-*p*-cresol as deoxygenation allowed product (Fig. 4−10).

4.3.8 2,5-Furandicarboxylic acid via hydroxy-methyl-furfural oxidation and CO_2-assisted furoate carboxylation

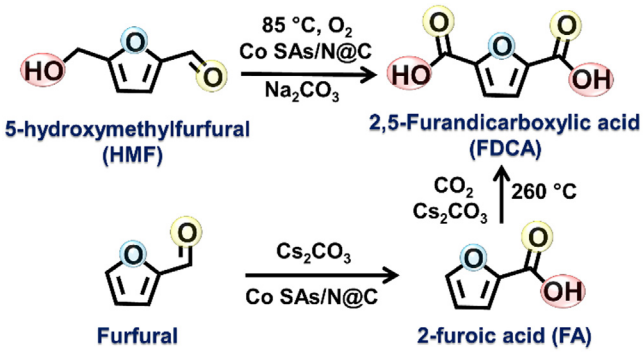

Transformation of biomass to oxygenates chemicals such as 2,5-furandicarboxylic acid (FDCA) which serves as a monomer to produce polyethylene furandicarboxylate (PEF) bioplastics can remove the dependency on petroleum-derived terephthalic acid [155]. The current route utilizes C6 sugar-derived HMF as a substrate for the synthesis of FDCA and

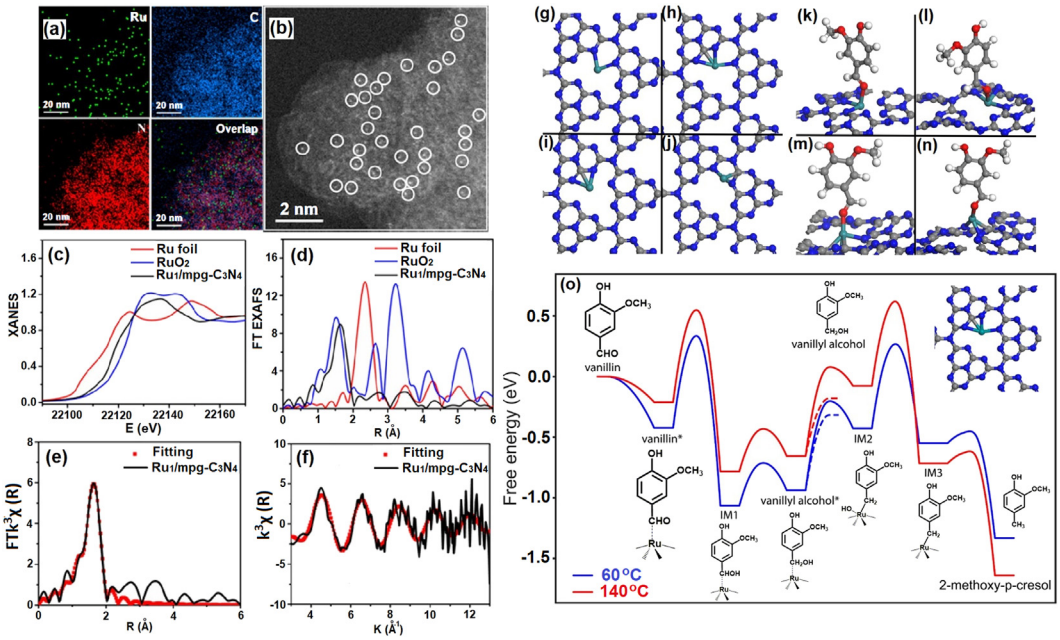

FIGURE 4–10 (a) EDX element maps of $Ru_1/mpg\text{-}C_3N_4$ showing the distributions of Ru, C, N, and their overlap (b) AC-HAADF-STEM images of the $Ru_1/mpg\text{-}C_3N_4$ sample, (c) XANES spectra at the Ru K-edge of $Ru_1/mpg\text{-}C_3N_4$, RuO_2, and Ru foil. (d) Fourier transform (FT) at the Ru K-edge of $Ru_1/mpg\text{-}C_3N_4$, RuO_2, and Ru foil. (e) and (f) Corresponding fits of the EXAFS spectrum of $Ru_1/mpg\text{-}C_3N_4$ in R space and K space, respectively. (g–j) Geometries of four different single-atom Ru catalyst structures on carbon nitride C, N, and Ru atoms are shown in gray, blue, and green, respectively. (k–n) Geometries of vanillin adsorption on the four single-atom Ru sites. (o) Free energy diagrams of vanillin hydrogenation to vanillyl alcohol and 2-methoxy-2-methoxy-*p*-cresol at 60°C (blue) and 140°C (red). The structures of reactant and products are shown above the energy profiles, while the intermediate state structures are shown below the energy profiles. The geometry of $Ru_1/mpg\text{-}C_3N_4$ is shown in the upper right. [154] *Reproduced with permission from S. Tian, Z. Wang, W. Gong, W. Chen, Q. Feng, Q. Xu, et al., Temperature-controlled selectivity of hydrogenation and hydrodeoxygenation in the conversion of biomass molecule by the $Ru_1/mpg\text{-}C_3N_4$ catalyst, J. Am. Chem. Soc., 140 (2018) 11161–11164. Copyright 2018 American Chemical Society.*

is inefficient due to poor conversion of lignocellulose-to-HMF and the instability of HMF [156,157]. Recently, the C5 route that uses a furfural derivative called 2-furoic acid (FA) and CO_2 as feedstocks to produce FDCA has attracted attention [158–160]. The lignin part of biomass is tedious to transform into chemicals due to phenolic structure and processability. The phenolic structure coordinates with metal ions and can be used for the synthesis of highly dispersed carbon-based catalysts. Zhou et al. synthesized cobalt/zinc–lignin (Co/Zn–L) complexes with lignin by taking advantage of metal–phenol coordination, which upon carbonization using dicyandiamide as a source of nitrogen produces N-doped carbon-supported Co single-atom catalysts (Co SACs/N@C) [161]. HR-TEM images show carbonaceous sheets and AC HAADF-STEM validates the distinct presence of isolated Co single-atoms. Furthermore, the XANES absorption edge between CoO and Co_3O_4 and the presence of a single peak

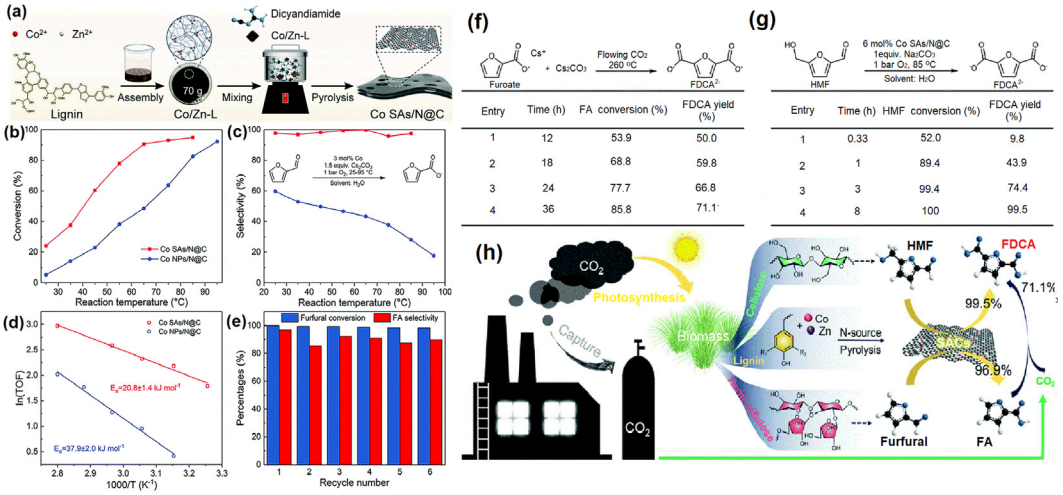

FIGURE 4–11 (a) Synthesis methodology of the Co SAs/N@C catalyst, catalytic performances of Co SAs/N@C for the oxidation of furfural to furoate, (b) conversion, and (c) selectivity of furfural oxidation at various temperatures over Co SAs/N@C and Co NPs/N@C; reaction conditions: 1 mmol furfural, 1.5 equiv. Cs_2CO_3, catalyst (^{n}Co/^{n}furfural = 0.03), 10 mL H_2O, 1 bar O_2, 11 h, (d) The Arrhenius plots of Co SAs/N@C and Co NPs/N@C. (e) Recycling of the Co SAs/N@C catalyst. Convergent production of FDCA from biomass and CO_2. (f) Synthesis of FDCA from furoate. (g) Synthesis of FDCA from HMF. (h) Conceptual diagram of convergent FDCA production from lignocellulosic biomass and CO_2. [161] *Reproduced with permission from H. Zhou, H. Xu, X. Wang, Y. Liu, Convergent production of 2, 5-furandicarboxylic acid from biomass and CO_2, Green. Chem., 21 (2019) 2923–2927. Copyright 2019 Royal Society of Chemistry.*

at 1.4 Å in EXAFS also evidenced the presence of atomically distributed cobalt atoms. Using Co SACs/N@C as catalyst and Cs_2CO_3 as a base, 90.5% conversion and 99.8% selectivity for furfural to FA oxidation was achieved at 65°C; while under identical conditions, Co nanoparticle catalysts (CoNPs/N@C) afforded only 48.6% conversion and 43.3% selectivity. The calculated activation energy (E_a) of Co SACs/N@C was found only at 20.8 kJ mol^{-1}, much lower than Co NPs/N@C (37.9 kJ mol^{-1}) and other reported noble metal catalysts, such as AuPd/Mg(OH)$_2$ (30.4 kJ mol^{-1}). The catalyst demonstrates extreme resiliency and 98.4% conversion, and 89.8% selectivity was observed even after six reuse experiments. An isotopic labeling experiment using ^{18}O labeled $H_2{}^{18}O$ and $^{18}O_2$ reveals that H_2O reacts with furfural to form geminal diol intermediates via base facilitation reversible hydration, while O_2 facilitates removal of protons from the active center of the catalyst due via accepting electrons. The reaction proceeds via an aldehyde-water shift (AWS) reaction pathway, reversible hydration reaction, and subsequent oxidative dehydrogenation. Furoate carboxylation using CO_2 in the presence of Cs_2CO_3 affords a 71.1% conversion and 82.9% selectivity for FDCA production (C5 route). Interestingly, the catalyst also demonstrated unprecedented activity for HMF oxidation (C6 route) to FDCA under a mild condition that illustrates the potential of a catalyst to catalyze a wide variety of biomass conversion reactions (Fig. 4–11).

4.3.9 Synthesis of cellulosic ethanol by facilitated methyl glycolate reduction

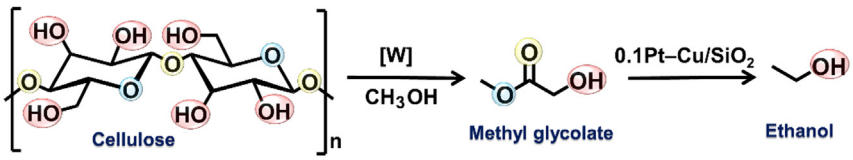

Ethanol is mostly produced from the fermentation of starch biomass from sugarcane, potato, corn, wheat, etc. Ethanol is widely used to produce chemicals, solvent, brewery, and fuel. Water-free ethanol also called "gasohol" with high octane numbers is blended with gasoline to reduce environmental impact. Since the 1980s, most gasoline-powered vehicles are compatible to use ethanol-blended gasoline and, in some countries/provinces (Brazil and United States), it is mandatory to blend 10% ethanol in gasoline [162]. The ethanol-gasoline blend called E85 or flex-fuel can have an ethanol percentage of 51% to 83% depending on geography and season [163,164]. The production of ethanol from biomass is advantageous as it reduced greenhouse gas emission but soaring food prices due to the usage of arable land are concerning points. Lignocellulosic biomass derived from agricultural wastes such as straw, corn stover, wood chips, and energy crops, such as switchgrass, can be used as feedstocks for producing ethanol without impacting the food chain supply [165].

Tao Zhang's group has reported that the cellulose can be converted to ethanol by a chemo-catalytic route by converting cellulose to methyl glycolate (MG) using methanol on a W-based catalyst followed by hydrogenation to ethanol over a supported copper catalyst [166]. However, the total yield of cellulose to ethanol conversion remains as low as 30%. Due to the high reaction temperature conversion of cellulose to methyl glycolate conversion remains low for this step. On the other hand, the yield of MG hydrogenation which proceeds at relatively low temperatures can be further improved by using a more efficient catalyst. Dimethyl oxalate (DMO) hydrogenation which simulates methyl glycolate hydrogenation has been widely investigated using a copper-based catalyst, but the formation of ethylene glycol is thermodynamically favored in comparison to DMO hydrogenation, as EG forms at 200°C, whereas ethanol forms at 260°C [167]. To improve the selectivity, platinum single-atoms isolated by copper on silica support were prepared to overcome the disadvantages of Pt nanoparticles that lead to C—C bond cleavage [168]. The Pt—Cu/SiO_2 single-atom alloy catalyst which has 0.1% Pt shows the increased intensity of a copper phyllosilicate peak in XRD and FTIR suggesting better interaction between Cu and SiO_2. Further, 0.1% Pt shows the highest dispersion of copper, confirmed by N_2O chemisorption (oxidize Cu to Cu_2O). Furthermore, H_2-TPD of 0.1Pt—Cu/SiO_2 shows a 20°C decrease in the Cu_2O reduction peak, suggesting Pt promotes the reduction of CuO. The CO adsorption followed by measurement of DRIFT spectra and XPS spectra including Cu LMM x-ray excited Auger spectroscopy (XAES) confirms that the incorporation of Pt increased the surface site density of Cu^+. In comparison to the Cu/SiO_2 catalyst which shows a maximum 68.8% selectivity at 250°C, the selectivity of

0.1Pt−Cu/SiO_2 was found at 76.7% at 230°C (approximately 20°C lower). It was speculated that MG dissociates at the Cu^+ sites while H_2 is dissociated as Pt atoms spillover to the neighboring Cu^0 atoms for subsequent hydrogenation. The 0.1Pt−Cu/SiO_2 catalyst showed a 7.7x higher TOF and stable activity up to 700 h of reaction with any deactivation (Fig. 4−12).

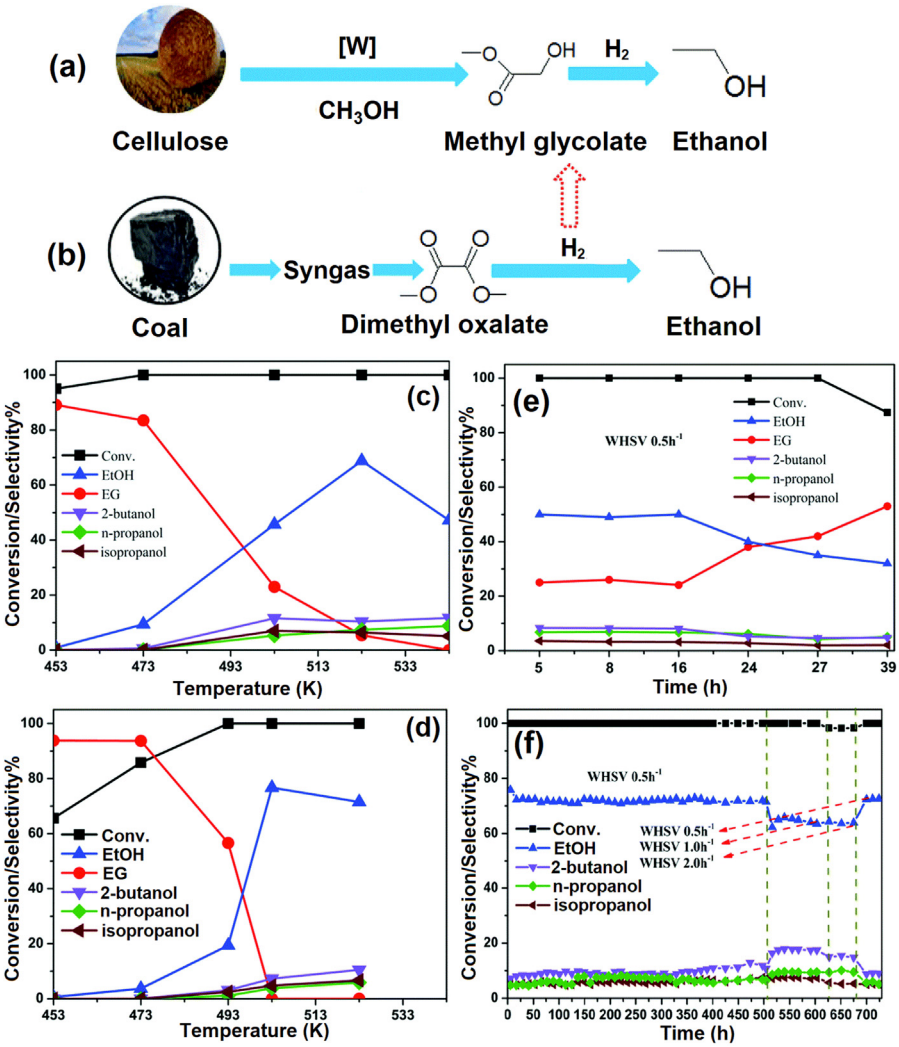

FIGURE 4–12 (a) Production of ethanol from lignocellulosic biomass through a two-step chemocatalytic approach; (b) production of ethanol from coal through dimethyl oxalate hydrogenation. Catalytic performances of (c) Cu/SiO_2, and (d) 0.1Pt−Cu/SiO_2 at different reaction temperatures. Reaction conditions: weight hour space velocity (WHSV) = 2.0 h^{-1}, H_2/MG = 120, and P(H_2) = 3 MPa. Catalytic performances versus time on stream over (e) Cu/SiO_2 (f) 0.1Pt−Cu/SiO_2 catalysts at 503 K. Reaction conditions: P(H_2) = 3 MPa and H_2/MG = 120 [168]. *Reproduced with permission from C. Yang, Z. Miao, F. Zhang, L. Li, Y. Liu, A. Wang, et al., Hydrogenolysis of methyl glycolate to ethanol over a Pt−Cu/SiO_2 single-atom alloy catalyst: a further step from cellulose to ethanol, Green. Chem., 20 (2018) 2142−2150. Copyright 2018 Royal Society of Chemistry.*

4.3.10 Selective decarboxylation of furfural to furan

The United States Department of Energy (US DoE) has ranked furfural and its derivatives among the top 30 biomass-derived platform chemicals [169]. The acid-catalyzed production of furfural from hemicellulose derived xylose is used at an industrial scale. Furfural serves as a substrate for the synthesis of high-volume products, such as polyols, which have direct applications in the polymer industry (polyesters, polyurethanes, and polyamides) [101,170]. However, a major fraction of furfural (~ 62%) is consumed to produce furfuryl alcohol, a precursor molecule for the synthesis of several chemicals, such as lubricants, ascorbic acid, furan-based resins, anticorrosive coatings, perfumes, and flavorings [171,172]. Existing technologies for the hydrogenation of furfural to furfuryl alcohol utilized toxic copper chromate catalysts at intense reaction temperature (200°C) and pressure (30 bar) which pose a disposal problem at the industrial scale [173]. Metal catalysts (Cu, Ru, Pt, etc.)on various supports have also been investigated as an alternative. Metals supported on MgO, CeO_2, and γ-Al_2O_3 were found to perform optimally for the selective hydrogenation of furfural to furfuryl alcohol [174–176]. DFT calculations suggest that furfural binds to copper via η_1(O)-aldehyde mode, which leads to a 100% selectivity of furfural to FA over a monometallic Cu/Al_2O_3 at 90°C [177]. To investigate the effect of metal size on product selectivity Islam et al. prepared a Cu/Al_2O_3 catalyst with 1% and 5% Cu loading, having high Cu dispersion and Cu nanoparticles, respectively [178]. XPS spectra showed Cu matched with + 1 oxidation state while the L_3VV Auger spectrum displayed a peak shift to lower kinetic energies, demonstrating the unique electronic character of Cu. Cu K-edge XANES and EXAFS validate the isolated atomically dispersed octahedral Cu^{2+} (O, $OH)_6$. The isolated and dimer Cu atoms in 1.0 wt.% Cu/Al_2O_3 catalysts promote the decarbonylation of furfural to furan because of the distinct interaction of atomic copper with furan ring. Cu nanoparticles catalyst in 5.0 wt.% Cu/Al_2O_3 leads to the formation of furfuryl alcohol. Interestingly, the introduction of sulfur in a catalyst using sulfate precursor has a detrimental effect on furfuryl alcohol selectivity, decreasing up to 0.8% from 94.6% and switching o an acetalization pathway and generating 2-furaldehyde dimethyl acetal (FDMA). (Fig. 4–13)

4.3.11 Selective production of γ-butyrolactone from succinic acid hydrogenation

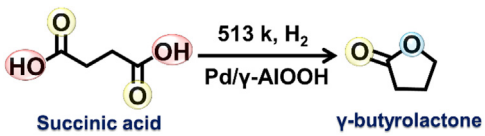

Succinic acid (SA) is one of the most demanding sugar-derived C4 dicarboxylate chemicals and is in the list of the top 12 bioderived chemicals [169]. It is a precursor of many industrial value chemicals and is commercially derived from the fermentation of sugars. Hydrogenation of succinic acid yields γ-butyrolactone (GBL), an important chemical intermediate and

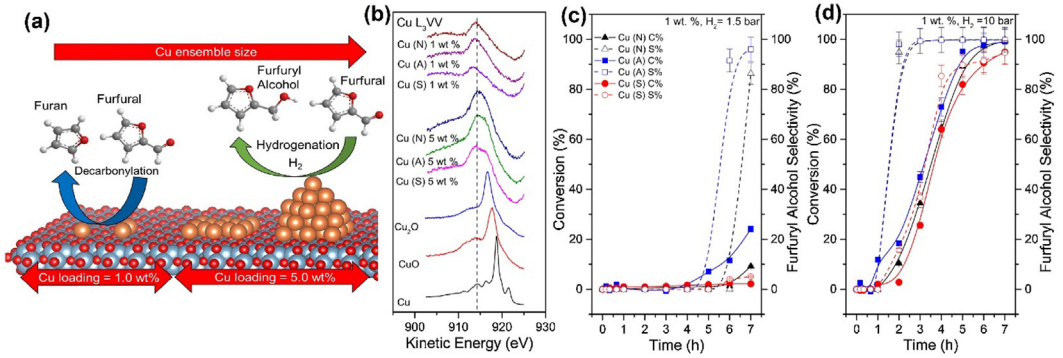

FIGURE 4–13 (a) A general outline of furfural decarboxylation to furan on a single-atom and furfuryl alcohol on multiatomic nanoparticles and (b) Cu L_3VV XAES spectra for the six Cu/Al_2O_3 catalysts and Cu, CuO and Cu_2O. The reaction profiles of furfural conversion and furfuryl alcohol selectivity using 1.0 wt.% Cu/Al_2O_3 catalysts selectivity at (c) 1.5 bar and (d) 10 bar of H_2, Conditions: temperature: 50°C, 600 rpm, and 30 mg of catalyst. Solid and dashed lines represent the conversion and selectivity to furfuryl alcohol, respectively [178]. *Reproduced with permission from M.J. Islam, M. Granollers Mesa, A. Osatiashtiani, M.J. Taylor, J.C. Manayil, C.M. Parlett, et al., The effect of metal precursor on copper phase dispersion and nanoparticle formation for the catalytic transformations of furfural, Appl. Catal. B: Environ., 273 (2020) 119062. Copyright 2020 Elsevier.*

solvent in fine chemicals, such as N-methyl-2-pyrrolidone (NMP) and 2-pyrrolidone. GBL can be further hydrogenated to 1,4-butanediol (BDO), or tetrahydrofuran (THF) [179–181]. BDO is a precursor to industrially important polymers such as polyurethane, polybutylene succinate (PBS), and polybutylene terephthalate (PBT), while THF is a versatile polar solvent [182]. On an industrial-scale γ-butyrolactone (GBL) is generally produced by direct hydrogenation of maleic anhydride [183]. Maleic anhydride is produced from fossil fuel feedstock, so replacing GBL production using succinic acid might provide an alternative route to use biomass for the production of drop-in chemicals at a low price and minimal environmental impact. Several Pd-based catalysts especially supported on mesoporous carbon and alumina have been found as an excellent catalyst for the hydrogenation of SA to GBL [184,185]. The hydrogenation of SA to GBL proceeds via the formation of succinic anhydride following C–O bond reduction and dehydration on acidic sites. In the second step, the oxidative hydrogenation of the CO bond leads to the formation of GBL on novel metal sites [186]. Alumina (Al_2O_3) possessing plenty of an acidic catalytic site has been used as support for Pd, but size heterogeneity leads to side reactions [186]. To overcome this drawback, Pd was atomically dispersed on γ-AlOOH nanosheets (Pd/γ-AlOOH) with 0.1, 0.5, and 1.0 wt.% Pd loading using a wet-impregnation method [187]. The SA to GBL conversion for 0.1 Pd/γ-AlOOH, 0.5 Pd/γ-AlOOH, and 1.0 Pd/γ-AlOOH was found to be 50.3%, 90.7% and 97.1% after 4 h while the corresponding selectivity was found to be 98.7%, 96.9%, and 93.8%, respectively. The TOF of 0.1 Pd/γ-AlOOH was obtained 305.4 cm^{-1}, which was much higher than 0.5 Pd/γ-AlOOH (175.7 cm^{-1}) and 1.0 Pd/γ-AlOOH (86.7 cm^{-1}). Based on the wt.% of Pd loading, the 0.1 Pd/γ-AlOOH displayed 1.9- and 10-times higher conversion than 0.5 Pd/γ-AlOOH and 1.0 Pd/γ-AlOOH, respectively. By considering the magic numbers for one atom (Pd_1), 13 atoms (Pd_{13}), and 55 atoms (Pd_{55}),

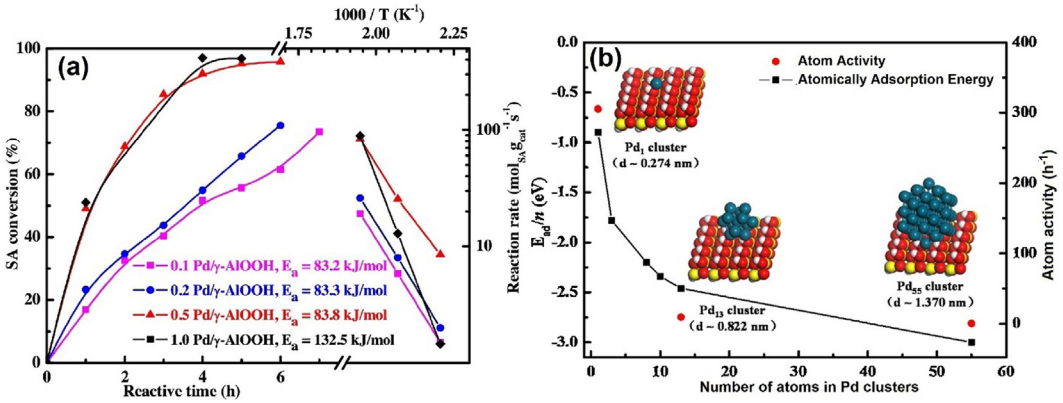

FIGURE 4–14 (a) The catalytic activity of SA hydrogenation and the Arrhenius plot of reaction rates over Pd/γ-AlOOH catalysts with different Pd loadings (b) Atom activity and adsorption energy for each Pd atom contribution in clusters. [187]. *Reproduced with permission from C. Zhang, L. Chen, H. Cheng, X. Zhu, Z. Qi, Atomically dispersed Pd catalysts for the selective hydrogenation of succinic acid to γ-butyrolactone, Catal. Today, 276 (2016) 55–61. Copyright 2016 Elsevier.*

the catalytic activity of supported single-atom was calculated to be 305.4 h^{-1}, 9.2 h^{-1} and 0.27 h^{-1} for SA hydrogenation, demonstrating the significance of a single-atom site. The kinetic tests reveal that the catalyst with low Pd loading and single-atom distribution (0.1 Pd/γ-AlOOH, 0.2 Pd/γ-AlOOH, and 0.5 Pd/γ-AlOOH) have almost same activation energies (Ea) of 83.5 ± 0.5 kJ mol^{-1}, while 1.0 Pd/γ-AlOOH with 28.2% single-atom contribution show an Ea = 132.5 kJ mol^{-1}, suggesting reaction process is driven by metallic Pd active sites. Using DFT calculations of Pd_n models (n = 1, 3, 8, 10, 13, and 55) supported on γ-AlOOH (010), the adsorption energies were calculated: the E_{ad}/n value for single-atom was −0.90 eV while for Pd_{55} cluster the value was −3.00 eV. The more negative value of Pd clusters suggests that in comparison to clusters, the group of individual atoms was more unstable, resulting in higher activity of the atomically dispersed catalyst (Fig. 4–14).

4.4 Conclusions

The abundant and renewable nature of biomass makes it an attractive alternative energy resource that can alleviate the problem of climate change and depleting fossil fuels. Currently, only a tiny fraction of biomass, specifically starch-rich grains/crops, is being utilized for alcohol/organic acid generation, but food security and the loss of biodiversity remain serious concerns. On the other hand, lignocellulosic biomass is widely available that has the potential to produce fuels and drop-in chemicals to replace fossil fuels. Conventional thermal valorization requires a high temperature and relies on stoichiometric hazardous catalysts to convert lignocellulosic biomass into chemicals. Additionally, the oxygen-rich nature of biomass and high moisture content affords a wide variety of products. With the advent of the modern catalytic system, the transformation of complex biomass and platform chemicals (derived from

valorization) to industrially important chemicals have become feasible. Unfortunately, most of the existing catalysts are facing the serious issue of poor selectivity and catalytic performance limiting their deployment of the system on a large scale. Size reduction of transition metal catalysts followed by anchoring on acidic or basic support was found to improve the performance; however, due to the presence of variable exposed sites and unequal size distribution, the problem of poor selectivity persists. The emergence of single-atom catalysts (SACs) has reciprocated the complete scenario as it offers ultimate selectivity due to the uniform distribution of single-atom active sites. The availability of each atomic site and interaction of single-atoms with support lead to a specific geometrical distribution that synergistically improves the performance of SACs. Designing single-atom catalysts using noble metals enhance the performance while at the same time make them recoverable and increase their stability under harsh conditions. In the present chapter we have revisited synthesis and application of noble and nonnoble metal SACs for biomass transformation into valuable chemicals. Only a handful of SACs fabricated on various supports, such as inorganic oxides, sulfides, and 2D materials, such as graphene and carbon nitrides using various metal centers, have been reported for the transformation of various biomass-derived platform chemicals into drop-in chemicals with unprecedented selectivity. Metal centers, such as Pt, Ru, Pd, Ir, Ni Cu, etc. supported on Al_2O_3, TiO_2, LDHs, graphene, and carbon nitride have been studied in detail for the conversion of platform chemicals that demonstrating $>95\%$ selectivity in almost every case. The entirely new properties, astonishing performance, selectivity, and amalgamated attributes of homogenous and heterogeneous catalysts make SACs the catalyst for the future which can overcome the issues of conventional catalyst systems.

Acknowledgments

The authors would like to thank the University of Calgary's Department of Chemical & Petroleum Engineering/Schulich School of Engineering and the University of Calgary CFREF fund for financial assistance.

References

[1] The World Counts Tons of CO_2 emitted into the atmosphere, 2020. https://www.theworldcounts.com/challenges/climate-change/global-warming/global-co2-emissions.

[2] B.J.S. Obama, The irreversible momentum of clean energy, Science 355 (2017) 126–129.

[3] A.E. Raftery, A. Zimmer, D.M. Frierson, R. Startz, P. Liu, Less than 2°C warming by 2100 unlikely, Nat. Clim. Change 7 (2017) 637.

[4] S. Chadburn, E. Burke, P. Cox, P. Friedlingstein, G. Hugelius, S. Westermann, An observation-based constraint on permafrost loss as a function of global warming, Nat. Clim. Change 7 (2017) 340–344.

[5] R. Warren, J. Price, E. Graham, N. Forstenhaeusler, J. VanDerWal, The projected effect on insects, vertebrates, and plants of limiting global warming to 1.5°C rather than 2°C, Science 360 (2018) 791–795.

[6] K.E. Trenberth, A. Dai, G. Van Der Schrier, P.D. Jones, J. Barichivich, K.R. Briffa, et al., Global warming and changes in drought, Nat. Clim. Change 4 (2014) 17–22.

[7] A. Cazenave, H.-B. Dieng, B. Meyssignac, K. Von Schuckmann, B. Decharme, E. Berthier, The rate of sea-level rise, Nat. Clim. Change 4 (2014) 358–361.

[8] P. Kumar, R. Boukherroub, K. Shankar, Sunlight-driven water-splitting using two-dimensional carbon based semiconductors, J. Mater. Chem. A 6 (2018) 12876–12931.

[9] P.C. Stern, B.K. Sovacool, T. Dietz, Towards a science of climate and energy choices, Nat. Clim. Change 6 (2016) 547–555.

[10] R.C. Armstrong, C. Wolfram, K.P. De Jong, R. Gross, N.S. Lewis, B. Boardman, et al., The frontiers of energy, Nat. Energy 1 (2016)15020.

[11] S. Chu, Y. Cui, N. Liu, The path towards sustainable energy, Nat. Mater. 16 (2017) 16–22.

[12] H. Ritchie, M. Roser, Renewable Energy, Our World Data (2020). Available from: https://ourworldindata.org/renewable-energy.

[13] U.S. Energy Information Administration https://www.eia.gov/outlooks/steo/report/global_oil.php.

[14] G.J. Kramer, B. Vermeer, Shell Oil Corp., The colours of energy: essays on the future of energy in society, 2014. https://www.shell.com/shared/energy-and-innovation/_jcr_content/par/textimage_599045333.stream/1461569264888/2c4d2cef2e60098f0c636e82c76ae38a2cd19297/the-colours-of-energy.pdf.

[15] G.J. Kramer, Challenges of a green future, Energy Sprawl Solutions, Springer, 2017, pp. 20–30.

[16] Y.M. Bar-On, R. Phillips, R. Milo, The biomass distribution on Earth, Proc. Natl. Acad. Sci. U. S. A. 115 (2018) 6506–6511.

[17] A. Thompson, Taking stock of life, Sci. Am. 319 (2018). 16–16.

[18] D.L. Sanchez, D.M. Kammen, A commercialization strategy for carbon-negative energy, Nat. Energy 1 (2016)15002.

[19] A. Corma, G.W. Huber, L. Sauvanaud, P. O'Connor, Biomass to chemicals: catalytic conversion of glycerol/water mixtures into acrolein, reaction network, J. Catal. 257 (2008) 163–171.

[20] M. Carus, L. Dammer, Á. Puente, A. Raschka, O. Arendt, Bio-based drop-in, smart drop-in and dedicated chemicals, Nova-Institut GmbH, Huerth, Germany, 2017.

[21] S. Singh, D. Singh, Biodiesel production through the use of different sources and characterization of oils and their esters as the substitute of diesel: a review, Renew. Sustain. Energy Rev. 14 (2010) 200–216.

[22] J.A. Ferreira, S. Agnihotri, M.J. Taherzadeh, Waste biorefinery, Sustainable Resource Recovery and Zero Waste Approaches, Elsevier, 2019, pp. 35–52.

[23] M. Balat, Production of bioethanol from lignocellulosic materials via the biochemical pathway: a review, Energy Convers. Manag. 52 (2011) 858–875.

[24] D.R. Keshwani, J.J. Cheng, Switchgrass for bioethanol and other value-added applications: a review, Bioresour. Technol. 100 (2009) 1515–1523.

[25] V. Balan, Current challenges in commercially producing biofuels from lignocellulosic biomass, Int. Sch. Res. Not. (2014)(2014).

[26] B. Thomas, M.C. Raj, J. Joy, A. Moores, G.L. Drisko, C. Sanchez, Nanocellulose, a versatile green platform: from biosources to materials and their applications, Chem. Rev. 118 (2018) 11575–11625.

[27] A.D. French, M.S. Cintrón, Cellulose polymorphy, crystallite size, and the Segal crystallinity index, Cellulose 20 (2013) 583–588.

[28] K. David, A.J. Ragauskas, Switchgrass as an energy crop for biofuel production: a review of its lignocellulosic chemical properties, Energy Environ. Sci. 3 (2010) 1182–1190.

[29] S.G. Wettstein, D.M. Alonso, E.I. Gürbüz, J.A. Dumesic, A roadmap for conversion of lignocellulosic biomass to chemicals and fuels, Curr. Opin. Chem. Eng. 1 (2012) 218–224.

[30] R.P. Overend, T. Milne, L. Mudge, Fundamentals of thermochemical biomass conversion, Springer Science and Business Media, 2012.

[31] H. Goyal, D. Seal, R. Saxena, Bio-fuels from thermochemical conversion of renewable resources: a review, Renew. Sustain. Energy Rev. 12 (2008) 504–517.

[32] L. Zhang, C.C. Xu, P. Champagne, Overview of recent advances in thermo-chemical conversion of biomass, Energy Convers. Manag. 51 (2010) 969−982.

[33] Y. Habibi, L.A. Lucia, O.J. Rojas, Cellulose nanocrystals: chemistry, self-assembly, and applications, Chem. Rev. 110 (2010) 3479−3500.

[34] X.Y. Ooi, W. Gao, H.C. Ong, H.V. Lee, J.C. Juan, W.H. Chen, et al., Overview on catalytic deoxygenation for biofuel synthesis using metal oxide supported catalysts, Renew. Sustain. Energy Rev. 112 (2019) 834−852.

[35] P. Sudarsanam, E. Peeters, E.V. Makshina, V.I. Parvulescu, B.F. Sels, Advances in porous and nanoscale catalysts for viable biomass conversion, Chem. Soc. Rev. 48 (2019) 2366−2421.

[36] Ml Besson, P. Gallezot, C. Pinel, Conversion of biomass into chemicals over metal catalysts, Chem. Rev. 114 (2014) 1827−1870.

[37] D.M. Alonso, J.Q. Bond, J.A. Dumesic, Catalytic conversion of biomass to biofuels, Green. Chem. 12 (2010) 1493−1513.

[38] T. Ennaert, J. Van Aelst, J. Dijkmans, R. De Clercq, W. Schutyser, M. Dusselier, et al., Potential and challenges of zeolite chemistry in the catalytic conversion of biomass, Chem. Soc. Rev. 45 (2016) 584−611.

[39] M. Stöcker, Biofuels and biomass-to-liquid fuels in the biorefinery: Catalytic conversion of lignocellulosic biomass using porous materials, Angew. Chem. Int. Ed. 47 (2008) 9200−9211.

[40] S. Vitolo, B. Bresci, M. Seggiani, M. Gallo, Catalytic upgrading of pyrolytic oils over HZSM-5 zeolite: behaviour of the catalyst when used in repeated upgrading−regenerating cycles, Fuel 80 (2001) 17−26.

[41] E.F. Iliopoulou, S. Stefanidis, K. Kalogiannis, A. Delimitis, A. Lappas, K. Triantafyllidis, Catalytic upgrading of biomass pyrolysis vapors using transition metal-modified ZSM-5 zeolite, Appl. Catal. B: Environ. 127 (2012) 281−290.

[42] J. Pang, J. Sun, M. Zheng, H. Li, Y. Wang, T. Zhang, Transition metal carbide catalysts for biomass conversion: A review, Appl. Catal. B: Environ. 254 (2019) 510−522.

[43] M.Y. Zheng, A.Q. Wang, N. Ji, J.F. Pang, X.D. Wang, T. Zhang, Transition metal−tungsten bimetallic catalysts for the conversion of cellulose into ethylene glycol, ChemSusChem 3 (2010) 63−66.

[44] P. Gallezot, Catalytic conversion of biomass: challenges and issues, ChemSusChem 1 (2008) 734−737.

[45] T.W. Walker, A.H. Motagamwala, J.A. Dumesic, G.W. Huber, Fundamental catalytic challenges to design improved biomass conversion technologies, J. Catal. 369 (2019) 518−525.

[46] L. Zhang, Y. Ren, W. Liu, A. Wang, T. Zhang, Single-atom catalyst: a rising star for green synthesis of fine chemicals, Natl Sci. Rev. 5 (2018) 653−672.

[47] A. Beniya, S. Higashi, Towards dense single-atom catalysts for future automotive applications, Nat. Catal. 2 (2019) 590−602.

[48] K.M. Alam, P. Kumar, P. Kar, U.K. Thakur, S. Zeng, K. Cui, et al., Enhanced charge separation in g-C_3N_4−BiOI heterostructures for visible light driven photoelectrochemical water splitting, Nanoscale Adv. 1 (2019) 1460−1471.

[49] H. Yan, C. Su, J. He, W. Chen, Single-atom catalysts and their applications in organic chemistry, J. Mater. Chem. A 6 (2018) 8793−8814.

[50] Y. Ren, Y. Tang, L. Zhang, X. Liu, L. Li, S. Miao, et al., Unraveling the coordination structure-performance relationship in Pt_1/Fe_2O_3 single-atom catalyst, Nat. Commun. 10 (2019) 1−9.

[51] A. Wang, J. Li, T. Zhang, Heterogeneous single-atom catalysis, Nat. Rev. Chem. 2 (2018) 65−81.

[52] B. Qiao, A. Wang, X. Yang, L.F. Allard, Z. Jiang, Y. Cui, et al., Single-atom catalysis of CO oxidation using Pt_1/FeO_x, Nat. Chem. 3 (2011) 634.

[53] R.T. Hannagan, G. Giannakakis, M. Flytzani-Stephanopoulos, E.C.H. Sykes, Single-atom alloy catalysis, Chem. Rev. 120 (2020) 12044−12088.

[54] J.M. Thomas, R. Raja, D.W. Lewis, Single-site heterogeneous catalysts, Angew. Chem. Int. Ed. 44 (2005) 6456−6482.

[55] L. Liu, A. Corma, Metal catalysts for heterogeneous catalysis: from single-atoms to nanoclusters and nanoparticles, Chem. Rev. 118 (2018) 4981−5079.

[56] Y. Chen, S. Ji, C. Chen, Q. Peng, D. Wang, Y. Li, Single-atom catalysts: synthetic strategies and electrochemical applications, Joule 2 (2018) 1242−1264.

[57] L. Jiao, H.-L. Jiang, Metal-organic-framework-based single-atom catalysts for energy applications, Chem 5 (2019) 786−804.

[58] J. Liu, Catalysis by supported single metal atoms, ACS Catal. 7 (2017) 34−59.

[59] Y. Qiu, Z. Wen, C. Jiang, X. Wu, R. Si, J. Bao, et al., Rational design of atomic layers of Pt anchored on Mo_2C nanorods for efficient hydrogen evolution over a wide pH range, Small 15 (2019) 1900014.

[60] H. Yan, H. Cheng, H. Yi, Y. Lin, T. Yao, C. Wang, et al., Single-atom Pd_1/graphene catalyst achieved by atomic layer deposition: remarkable performance in selective hydrogenation of 1, 3-butadiene, J. Am. Chem. Soc. 137 (2015) 10484−10487.

[61] S. Yang, J. Kim, Y.J. Tak, A. Soon, H. Lee, Single-atom catalyst of platinum supported on titanium nitride for selective electrochemical reactions, Angew. Chem. 128 (2016) 2098−2102.

[62] B. Qiao, J.-X. Liang, A. Wang, C.-Q. Xu, J. Li, T. Zhang, et al., Ultrastable single-atom gold catalysts with strong covalent metal-support interaction (CMSI), Nano Res. 8 (2015) 2913−2924.

[63] R. Lang, W. Xi, J.-C. Liu, Y.-T. Cui, T. Li, A.F. Lee, et al., Non defect-stabilized thermally stable single-atom catalyst, Nat. Commun. 10 (2019)234.

[64] R. Lang, T. Li, D. Matsumura, S. Miao, Y. Ren, Y.T. Cui, et al., Hydroformylation of olefins by a rhodium single-atom catalyst with activity comparable to RhCl $(PPh_3)_3$, Angew. Chem. Int. Ed. 55 (2016) 16054−16058.

[65] K. Harrath, X. Yu, H. Xiao, J. Li, The key role of support surface hydrogenation in the CH_4 to CH_3OH selective oxidation by a ZrO_2-supported single-atom catalyst, ACS Catal. 9 (2019) 8903−8909.

[66] J. Lin, A. Wang, B. Qiao, X. Liu, X. Yang, X. Wang, et al., Remarkable performance of Ir_1/FeO_x single-atom catalyst in water gas shift reaction, J. Am. Chem. Soc. 135 (2013) 15314−15317.

[67] P. Ganguly, M. Harb, Z. Cao, L. Cavallo, A. Breen, S. Dervin, et al., 2D nanomaterials for photocatalytic hydrogen production, ACS Energy Lett. 4 (2019) 1687−1709.

[68] A.J. Mannix, B. Kiraly, M.C. Hersam, N.P. Guisinger, Synthesis and chemistry of elemental 2D materials, Nat. Rev. Chem. 1 (2017)0014.

[69] S. Manzeli, D. Ovchinnikov, D. Pasquier, O.V. Yazyev, A. Kis, 2D transition metal dichalcogenides, Nat. Rev. Mater. 2 (2017) 17033.

[70] D. Zhao, Z. Chen, W. Yang, S. Liu, X. Zhang, Y. Yu, et al., MXene (Ti_3C_2) vacancy-confined single-atom catalyst for efficient functionalization of CO_2, J. Am. Chem. Soc. 141 (2019) 4086−4093.

[71] Y. Lou, Y. Zheng, X. Li, N. Ta, J. Xu, Y. Nie, et al., Pocketlike active site of Rh_1/MoS_2 single-atom catalyst for selective crotonaldehyde hydrogenation, J. Am. Chem. Soc. 141 (2019) 19289−19295.

[72] H. Zhang, L. Yu, T. Chen, W. Zhou, X.W. Lou, Surface modulation of hierarchical MoS_2 nanosheets by Ni single-atoms for enhanced electrocatalytic hydrogen evolution, Adv. Funct. Mater. 28 (2018) 1807086.

[73] X. Wang, Y. Zhang, H. Si, Q. Zhang, J. Wu, L. Gao, et al., Single-atom vacancy defect to trigger high-efficiency hydrogen evolution of MoS_2, J. Am. Chem. Soc. 142 (2020) 4298−4308.

[74] E. Meza, R.E. Diaz, C.W. Li, Solution-phase activation and functionalization of colloidal WS_2 nanosheets with Ni single-atoms, ACS Nano 14 (2020) 2238−2247.

[75] J. Zhang, Y. Zhao, X. Guo, C. Chen, C.-L. Dong, R.-S. Liu, et al., Single platinum atoms immobilized on an MXene as an efficient catalyst for the hydrogen evolution reaction, Nat. Catal. 1 (2018) 985−992.

[76] P. Kumar, E. Vahidzadeh, U.K. Thakur, P. Kar, K.M. Alam, A. Goswami, et al., C_3N_5: a low bandgap semiconductor containing an azo-linked carbon nitride framework for photocatalytic, photovoltaic and adsorbent applications, J. Am. Chem. Soc. 141 (2019) 5415−5436.

[77] K. Bhattacharyya, A. Datta, Visible light driven efficient metal free single-atom catalyst supported on nanoporous carbon nitride for nitrogen fixation, Phys. Chem. Chem. Phys. 21 (2019) 12346−12352.

[78] Z. Chen, E. Vorobyeva, S. Mitchell, E. Fako, N. López, S.M. Collins, et al., Single-atom heterogeneous catalysts based on distinct carbon nitride scaffolds, Natl Sci. Rev. 5 (2018) 642−652.

[79] X. Li, P. Cui, W. Zhong, J. Li, X. Wang, Z. Wang, et al., Graphitic carbon nitride supported single-atom catalysts for efficient oxygen evolution reaction, Chem. Commun. 52 (2016) 13233−13236.

[80] M. Grilc, G. Veryasov, B. Likozar, A. Jesih, J. Levec, Hydrodeoxygenation of solvolysed lignocellulosic biomass by unsupported MoS_2, MoO_2, Mo_2C and WS_2 catalysts, Appl. Catal. B: Environ. 163 (2015) 467−477.

[81] X. Chang, A.F. Liu, B. Cai, J.Y. Luo, H. Pan, Y.B. Huang, Catalytic transfer hydrogenation of furfural to 2-methylfuran and 2-methyltetrahydrofuran over bimetallic copper−palladium catalysts, ChemSusChem 9 (2016) 3330−3337.

[82] S. Kim, E.E. Kwon, Y.T. Kim, S. Jung, H.J. Kim, G.W. Huber, et al., Recent advances in hydrodeoxygenation of biomass-derived oxygenates over heterogeneous catalysts, Green. Chem. 21 (2019) 3715−3743.

[83] J. Luo, M. Monai, H. Yun, L. Arroyo-Ramírez, C. Wang, C.B. Murray, et al., The H_2 pressure dependence of hydrodeoxygenation selectivities for furfural over Pt/C catalysts, Catal. Lett. 146 (2016) 711−717.

[84] K. Murugappan, E.M. Anderson, D. Teschner, T.E. Jones, K. Skorupska, Y. Román-Leshkov, Operando NAP-XPS unveils differences in MoO_3 and Mo_2C during hydrodeoxygenation, Nat. Catal. 1 (2018) 960−967.

[85] A.V. Mironenko, D.G. Vlachos, Conjugation-driven "reverse Mars−van Krevelen"-type radical mechanism for low-temperature C−O bond activation, J. Am. Chem. Soc. 138 (2016) 8104−8113.

[86] C. Zhang, H. He, K.-i Tanaka, Catalytic performance and mechanism of a Pt/TiO_2 catalyst for the oxidation of formaldehyde at room temperature, Appl. Catal. B: Environ. 65 (2006) 37−43.

[87] C. Wang, A.V. Mironenko, A. Raizada, T. Chen, X. Mao, A. Padmanabhan, et al., Mechanistic study of the direct hydrodeoxygenation of m-cresol over WO_x-decorated Pt/C catalysts, ACS Catal. 8 (2018) 7749−7759.

[88] M.B. Griffin, G.A. Ferguson, D.A. Ruddy, M.J. Biddy, G.T. Beckham, J.A. Schaidle, Role of the support and reaction conditions on the vapor-phase deoxygenation of m-cresol over Pt/C and Pt/TiO_2 catalysts, ACS Catal. 6 (2016) 2715−2727.

[89] J. Fu, J. Lym, W. Zheng, K. Alexopoulos, A.V. Mironenko, N. Li, et al., C−O bond activation using ultralow loading of noble metal catalysts on moderately reducible oxides, Nat. Catal. 3 (2020) 446−453.

[90] F. Melligan, M. Hayes, W. Kwapinski, J. Leahy, Hydro-pyrolysis of biomass and online catalytic vapor upgrading with Ni-ZSM-5 and Ni-MCM-41, Energy fuels 26 (2012) 6080−6090.

[91] A.S. Ouedraogo, P.R. Bhoi, Recent progress of metals supported catalysts for hydrodeoxygenation of biomass derived pyrolysis oil, J. Clean. Prod. 253 (2020) 119957.

[92] C. Yang, L. Jia, C. Chen, G. Liu, W. Fang, Bio-oil from hydro-liquefaction of Dunaliella salina over Ni/REHY catalyst, Bioresour. Technol. 102 (2011) 4580−4584.

[93] G. Liang, H. Cheng, W. Li, L. He, Y. Yu, F. Zhao, Selective conversion of microcrystalline cellulose into hexitols on nickel particles encapsulated within ZSM-5 zeolite, Green. Chem. 14 (2012) 2146−2149.

[94] D. Chen, W. Wang, C. Liu, Hydrogen production through glycerol steam reforming over beehive-biomimetic graphene-encapsulated nickel catalysts, Renew. Energy 145 (2020) 2647−2657.

[95] T. Möller, W. Ju, A. Bagger, X. Wang, F. Luo, T.N. Thanh, et al., Efficient CO_2 to CO electrolysis on solid Ni−N−C catalysts at industrial current densities, Energy Environ. Sci. 12 (2019) 640−647.

[96] J. Li, S. Ghoshal, W. Liang, M.-T. Sougrati, F. Jaouen, B. Halevi, et al., Structural and mechanistic basis for the high activity of Fe−N−C catalysts toward oxygen reduction, Energy Environ. Sci. 9 (2016) 2418−2432.

[97] W. Ju, A. Bagger, X. Wang, Y. Tsai, F. Luo, T. Möller, et al., Unraveling mechanistic reaction pathways of the electrochemical CO_2 reduction on Fe−N−C single-site catalysts, ACS Energy Lett. 4 (2019) 1663−1671.

[98] W. Liu, Y. Chen, H. Qui, L. Zhang, W. Yan, X. Liu, et al., A durable nickel single-atom catalyst for hydrogenation reactions and cellulose valorization under harsh conditions, Angew. Chem. 130 (2018) 7189−7193.

[99] T. Ikuno, J. Zheng, A. Vjunov, M. Sanchez-Sanchez, M.A. Ortuño, D.R. Pahls, et al., Methane oxidation to methanol catalyzed by Cu-oxo clusters stabilized in NU-1000 metal−organic framework, J. Am. Chem. Soc. 139 (2017) 10294−10301.

[100] A. Sharma, M. Varshney, H.J. Shin, B.-H. Lee, K.H. Chae, S.O. Won, Effect of Cu insertion on structural, local electronic/atomic structure and photocatalyst properties of TiO_2, ZnO and $Ni(OH)_2$ nanostructures: XANES-EXAFS study, Mater. Chem. Phys. 191 (2017) 129−144.

[101] J.P. Lange, E. Van Der Heide, J. van Buijtenen, R. Price, Furfural—a promising platform for lignocellulosic biofuels, ChemSusChem 5 (2012) 150−166.

[102] S. Dutta, S. De, B. Saha, M.I. Alam, Advances in conversion of hemicellulosic biomass to furfural and upgrading to biofuels, Catal. Sci. Technol. 2 (2012) 2025−2036.

[103] R. Rao, A. Dandekar, R. Baker, M. Vannice, Properties of copper chromite catalysts in hydrogenation reactions, J. Catal. 171 (1997) 406−419.

[104] M.J. Taylor, L.J. Durndell, M.A. Isaacs, C.M. Parlett, K. Wilson, A.F. Lee, et al., Highly selective hydrogenation of furfural over supported Pt nanoparticles under mild conditions, Appl. Catal. B: Environ. 180 (2016) 580−585.

[105] X. Chen, L. Zhang, B. Zhang, X. Guo, X. Mu, Highly selective hydrogenation of furfural to furfuryl alcohol over Pt nanoparticles supported on g-C_3N_4 nanosheets catalysts in water, Sci. Rep. 6 (2016)28558.

[106] N.S. Date, A.M. Hengne, K.-W. Huang, R.C. Chikate, C.V. Rode, Single pot selective hydrogenation of furfural to 2-methylfuran over carbon supported iridium catalysts, Green. Chem. 20 (2018) 2027−2037.

[107] S. Tian, W. Gong, W. Chen, N. Lin, Y. Zhu, Q. Feng, et al., Regulating the catalytic performance of single-atomic-site IR catalyst for biomass conversion by metal−support interactions, ACS Catal. 9 (2019) 5223−5230.

[108] W. Cao, L. Lin, H. Qi, Q. He, Z. Wu, A. Wang, et al., In-situ synthesis of single-atom Ir by utilizing metal-organic frameworks: An acid-resistant catalyst for hydrogenation of levulinic acid to γ-valerolactone, J. Catal. 373 (2019) 161−172.

[109] M. Yabushita, H. Kobayashi, A. Fukuoka, Catalytic transformation of cellulose into platform chemicals, Appl. Catal. B: Environ. 145 (2014) 1−9.

[110] N. Hassan, A. Jalil, C. Hitam, D. Vo, W. Nabgan, Biofuels and renewable chemicals production by catalytic pyrolysis of cellulose: a review, Environ. Chem. Lett. 18 (2020) 1625−1648.

[111] A. Yamaguchi, N. Mimura, M. Shirai, O. Sato, Cascade utilization of biomass: strategy for conversion of cellulose, hemicellulose, and lignin into useful chemicals, ACS Sustain. Chem. Eng. 7 (2019) 10445−10451.

[112] P.K. Rout, A.D. Nannaware, O. Prakash, A. Kalra, R. Rajasekharan, Synthesis of hydroxymethylfurfural from cellulose using green processes: A promising biochemical and biofuel feedstock, Chem. Eng. Sci. 142 (2016) 318−346.

[113] B.P. Pinto, A.L.L. Fortuna, C.P. Cardoso, C.J. Mota, Hydrogenation of levulinic acid (LA) to γ-Valerolactone (GVL) over Ni−Mo/C catalysts and water-soluble solvent systems, Catal. Lett. 147 (2017) 751−757.

[114] S.G. Wettstein, J.Q. Bond, D.M. Alonso, H.N. Pham, A.K. Datye, J.A. Dumesic, RuSn bimetallic catalysts for selective hydrogenation of levulinic acid to γ-valerolactone, Appl. Catal. B: Environ. 117 (2012) 321−329.

[115] W. Cao, W. Luo, H. Ge, Y. Su, A. Wang, T. Zhang, UiO-66 derived Ru/ZrO_2@C as a highly stable catalyst for hydrogenation of levulinic acid to γ-valerolactone, Green. Chem. 19 (2017) 2201−2211.

[116] P.P. Upare, J.-M. Lee, D.W. Hwang, S.B. Halligudi, Y.K. Hwang, J.-S. Chang, Selective hydrogenation of levulinic acid to γ-valerolactone over carbon-supported noble metal catalysts, J. Ind. Eng. Chem. 17 (2011) 287−292.

[117] W. Luo, M. Sankar, A.M. Beale, Q. He, C.J. Kiely, P.C. Bruijnincx, et al., High performing and stable supported nano-alloys for the catalytic hydrogenation of levulinic acid to γ-valerolactone, Nat. Commun. 6 (2015)6540.

[118] J. Ftouni, A. Muñoz-Murillo, A. Goryachev, J.P. Hofmann, E.J. Hensen, L. Lu, et al., ZrO_2 is preferred over TiO_2 as support for the Ru-catalyzed hydrogenation of levulinic acid to γ-valerolactone, ACS Catal. 6 (2016) 5462−5472.

[119] W. Li, J.-H. Xie, H. Lin, Q.-L. Zhou, Highly efficient hydrogenation of biomass-derived levulinic acid to γ-valerolactone catalyzed by iridium pincer complexes, Green. Chem. 14 (2012) 2388−2390.

[120] H. Ou, L. Lin, Y. Zheng, P. Yang, Y. Fang, X. Wang, Tri-s-triazine-based crystalline carbon nitride nanosheets for an improved hydrogen evolution, Adv. Mater. 29 (2017) 1700008.

[121] Y. Su, H.M. Brown, X. Huang, X.-d Zhou, J.E. Amonette, Z.C. Zhang, Single-step conversion of cellulose to 5-hydroxymethylfurfural (HMF), a versatile platform chemical, Appl. Catal. A: Gen. 361 (2009) 117−122.

[122] J. Nie, J. Xie, H. Liu, Efficient aerobic oxidation of 5-hydroxymethylfurfural to 2, 5-diformylfuran on supported Ru catalysts, J. Catal. 301 (2013) 83−91.

[123] Z. Yuan, B. Liu, P. Zhou, Z. Zhang, Q. Chi, Aerobic oxidation of biomass-derived 5-hydroxymethylfurfural to 2, 5-diformylfuran with cesium-doped manganese dioxide, Catal. Sci. Technol. 8 (2018) 4430−4439.

[124] Y. Liu, T. Gan, Q. He, H. Zhang, X. He, H. Ji, Catalytic oxidation of 5-hydroxymethylfurfural to 2, 5-diformylfuran over atomically dispersed ruthenium catalysts, Ind. Eng. Chem. Res. 59 (2020) 4333−4337.

[125] G.D. Yadav, R.V. Sharma, Biomass derived chemicals: Environmentally benign process for oxidation of 5-hydroxymethylfurfural to 2, 5-diformylfuran by using nano-fibrous Ag-OMS-2-catalyst, Appl. Catal. B: Environ. 147 (2014) 293−301.

[126] S. Wang, Z. Zhang, B. Liu, J. Li, Environmentally friendly oxidation of biomass derived 5-hydroxymethylfurfural into 2, 5-diformylfuran catalyzed by magnetic separation of ruthenium catalyst, Ind. Eng. Chem. Res. 53 (2014) 5820−5827.

[127] P. Okoye, B. Hameed, Review on recent progress in catalytic carboxylation and acetylation of glycerol as a byproduct of biodiesel production, Renew. Sustain. Energy Rev. 53 (2016) 558−574.

[128] N. Kolesárová, M. Hutňan, I. Bodík, V. Špalková, Utilization of biodiesel by-products for biogas production, BioMed. Res. Int. 2011 (2011)26798.

[129] N.A.A. Adnan, S.N. Suhaimi, S. Abd-Aziz, M.A. Hassan, L.-Y. Phang, Optimization of bioethanol production from glycerol by Escherichia coli SS1, Renew. Energy 66 (2014) 625−633.

[130] N. Pachauri, B. He, Value-added utilization of crude glycerol from biodiesel production: a survey of current research activities, Proceedings of the ASABE Annual International Meeting, Citeseer, 2006, 1−16.

[131] M.R. Monteiro, C.L. Kugelmeier, R.S. Pinheiro, M.O. Batalha, A. da Silva, César, Glycerol from biodiesel production: Technological paths for sustainability, Renew. Sustain. Energy Rev. 88 (2018) 109−122.

[132] D. Liu, H. Liu, Y. Sun, R. Lin, J. Hao, Method for producing 1, 3-propanediol using crude glycerol, a by-product from biodiesel production, U.S. Patent No. 8,486,673. 16 Jul. 2013.

[133] F. Yang, M.A. Hanna, R. Sun, Value-added uses for crude glycerol—a byproduct of biodiesel production, Biotechnol. Biofuels 5 (2012) 1—10.

[134] U.I. Nda-Umar, I. Ramli, Y.H. Taufiq-Yap, E.N. Muhamad, An overview of recent research in the conversion of glycerol into biofuels, fuel additives and other bio-based chemicals, Catalysts 9 (2019) 15.

[135] G. Shi, J. Xu, Z. Song, Z. Cao, K. Jin, S. Xu, et al., Selective hydrogenolysis of glycerol to 1, 3-propanediol over Pt-WO_x/SAPO-34 catalysts, Mol. Catal. 456 (2018) 22—30.

[136] J. Chaminand, L. aurent Djakovitch, P. Gallezot, P. Marion, C. Pinel, C. Rosier, Glycerol hydrogenolysis on heterogeneous catalysts, Green. Chem. 6 (2004) 359—361.

[137] A. Talebian-Kiakalaieh, N.A.S. Amin, K. Rajaei, S. Tarighi, Oxidation of bio-renewable glycerol to value-added chemicals through catalytic and electro-chemical processes, Appl. Energy 230 (2018) 1347—1379.

[138] N. Vivek, R. Sindhu, A. Madhavan, A.J. Anju, E. Castro, V. Faraco, et al., Recent advances in the production of value added chemicals and lipids utilizing biodiesel industry generated crude glycerol as a substrate—metabolic aspects, challenges and possibilities: an overview, Bioresour. Technol. 239 (2017) 507—517.

[139] Y. Zheng, X. Chen, Y. Shen, Commodity chemicals derived from glycerol, an important biorefinery feedstock, Chem. Rev. 108 (2008) 5253—5277.

[140] K.S. Avasthi, R.N. Reddy, S. Patel, Challenges in the production of hydrogen from glycerol—a biodiesel byproduct via steam reforming process, Procedia Eng. 51 (2013) 423—429.

[141] S.S. Yazdani, R. Gonzalez, Anaerobic fermentation of glycerol: a path to economic viability for the biofuels industry, Curr. Opin. Biotechnol. 18 (2007) 213—219.

[142] A.N. Ardila, M.A. Sánchez-Castillo, T.A. Zepeda, A.L. Villa, G.A. Fuentes, Glycerol hydrodeoxygenation to 1, 2-propanediol catalyzed by CuPd/TiO_2-Na, Appl. Catal. B: Environ. 219 (2017) 658—671.

[143] M. Lee, Y.K. Hwang, J.-S. Chang, H.-J. Chae, D.W. Hwang, Vapor-phase hydrogenolysis of glycerol to 1, 2-propanediol using a chromium-free Ni-Cu-SiO_2 nanocomposite catalyst, Catal. Commun. 84 (2016) 5—10.

[144] N.D. Kim, J.R. Park, D.S. Park, B.K. Kwak, J. Yi, Promoter effect of Pd in $CuCr_2O_4$ catalysts on the hydrogenolysis of glycerol to 1, 2-propanediol, Green. Chem. 14 (2012) 2638—2646.

[145] A.J. Pamphile-Adrián, P.P. Florez-Rodriguez, M.H.M. Pires, G. Perez, F.B. Passos, Selective hydrogenolysis of glycerol over Ir-Ni bimetallic catalysts, Catal. Today 289 (2017) 302—308.

[146] J. Feng, B. Xu, W.D. Jiang, W. Xiong, J.B. Wang, Hydrogenolysis of glycerol on supported Ru-Co bimetallic catalysts, Advanced Materials Research, Trans. Tech. Publ. (2012) 297—300.

[147] S. Zhu, X. Gao, Y. Zhu, Y. Zhu, H. Zheng, Y. Li, Promoting effect of boron oxide on Cu/SiO_2 catalyst for glycerol hydrogenolysis to 1, 2-propanediol, J. Catal. 303 (2013) 70—79.

[148] I. Gandarias, P. Arias, J. Requies, M. Güemez, J. Fierro, Hydrogenolysis of glycerol to propanediols over a Pt/ASA catalyst: The role of acid and metal sites on product selectivity and the reaction mechanism, Appl. Catal. B: Environ. 97 (2010) 248—256.

[149] X. Zhang, G. Cui, H. Feng, L. Chen, H. Wang, B. Wang, et al., Platinum—copper single-atom alloy catalysts with high performance towards glycerol hydrogenolysis, Nat. Commun. 10 (2019)5812.

[150] B. Pongthawornsakun, P. Kaewsuanjik, P. Kittipreechakun, M. Ratova, P. Kelly, O. Mekasuwandumrong, et al., Deposition of Pt nanoparticles on TiO_2 by pulsed direct current magnetron sputtering for selective hydrogenation of vanillin to vanillyl alcohol, Catal. Today (2019).

[151] J. Santos, M. Alda-Onggar, V. Fedorov, M. Peurla, K. Eränen, P. Mäki-Arvela, et al., Hydrodeoxygenation of vanillin over carbon supported metal catalysts, Appl. Catal. A: Gen. 561 (2018) 137—149.

[152] S.C. Shit, P. Koley, B. Joseph, C. Marini, L. Nakka, J. Tardio, et al., Porous organic polymer-driven evolution of high-performance cobalt phosphide hybrid nanosheets as vanillin hydrodeoxygenation catalyst, ACS Appl. Mater. Interfaces 11 (2019) 24140—24153.

[153] S.C. Shit, R. Singuru, S. Pollastri, B. Joseph, B.S. Rao, N. Lingaiah, et al., Cu−Pd bimetallic nanoalloy anchored on a N-rich porous organic polymer for high-performance hydrodeoxygenation of biomass-derived vanillin, Catal. Sci. Technol. 8 (2018) 2195−2210.

[154] S. Tian, Z. Wang, W. Gong, W. Chen, Q. Feng, Q. Xu, et al., Temperature-controlled selectivity of hydrogenation and hydrodeoxygenation in the conversion of biomass molecule by the Ru_1/mpg-C_3N_4 catalyst, J. Am. Chem. Soc. 140 (2018) 11161−11164.

[155] L. Wei, J. Zhang, W. Deng, S. Xie, Q. Zhang, Y. Wang, Catalytic transformation of 2, 5-furandicarboxylic acid to adipic acid over niobic acid-supported Pt nanoparticles, Chem. Commun. 55 (2019) 8013−8016.

[156] M. Sajid, X. Zhao, D. Liu, Production of 2, 5-furandicarboxylic acid (FDCA) from 5-hydroxymethylfurfural (HMF): recent progress focusing on the chemical-catalytic routes, Green. Chem. 20 (2018) 5427−5453.

[157] S. Dutta, S. De, B. Saha, A brief summary of the synthesis of polyester building-block chemicals and biofuels from 5-hydroxymethylfurfural, ChemPlusChem 77 (2012) 259.

[158] K.A. Payne, S.A. Marshall, K. Fisher, M.J. Cliff, D.M. Cannas, C. Yan, et al., Enzymatic carboxylation of 2-furoic acid yields 2, 5-furandicarboxylic acid (FDCA), ACS Catal. 9 (2019) 2854−2865.

[159] S. Zhang, J. Lan, Z. Chen, G. Yin, G. Li, Catalytic synthesis of 2, 5-furandicarboxylic acid from furoic acid: transformation from C5 platform to C6 derivatives in biomass utilizations, ACS Sustain. Chem. Eng. 5 (2017) 9360−9369.

[160] A. Banerjee, G.R. Dick, T. Yoshino, M.W. Kanan, Carbon dioxide utilization via carbonate-promoted C−H carboxylation, Nature 531 (2016) 215−219.

[161] H. Zhou, H. Xu, X. Wang, Y. Liu, Convergent production of 2, 5-furandicarboxylic acid from biomass and CO_2, Green. Chem. 21 (2019) 2923−2927.

[162] F. Liu, M.D. Short, J.P. Alvarez-Gaitan, X. Guo, J. Duan, C. Saint, et al., Environmental life cycle assessment of lignocellulosic ethanol-blended fuels: A case study, J. Clean. Prod. 245 (2020) 118933.

[163] J. Anderson, D. DiCicco, J. Ginder, U. Kramer, T. Leone, H. Raney-Pablo, et al., High octane number ethanol−gasoline blends: Quantifying the potential benefits in the United States, Fuel 97 (2012) 585−594.

[164] D.N. Koplow, Biofuels−at what cost? Government Support for Ethanol and Biodiesel in the United States, International Institute for Sustainable Development, Geneva, 2006.

[165] D. Sharma, A. Saini, Introduction to Lignocellulosic Ethanol, Lignocellulosic Ethanol Production from a Biorefinery Perspective, Springer, 2020, pp. 1−21.

[166] G. Xu, A. Wang, J. Pang, X. Zhao, J. Xu, N. Lei, et al., Chemocatalytic conversion of cellulosic biomass to methyl glycolate, ethylene glycol, and ethanol, ChemSusChem 10 (2017) 1390−1394.

[167] Y. Wang, Y. Shen, Y. Zhao, J. Lv, S. Wang, X. Ma, Insight into the balancing effect of active Cu species for hydrogenation of carbon−oxygen bonds, ACS Catal. 5 (2015) 6200−6208.

[168] C. Yang, Z. Miao, F. Zhang, L. Li, Y. Liu, A. Wang, et al., Hydrogenolysis of methyl glycolate to ethanol over a Pt−Cu/SiO_2 single-atom alloy catalyst: a further step from cellulose to ethanol, Green. Chem. 20 (2018) 2142−2150.

[169] J.E. Holladay, J.F. White, J.J. Bozell, D. Johnson, Top value-added chemicals from biomass-Volume II—Results of screening for potential candidates from biorefinery lignin, Pacific Northwest National Lab. (PNNL), Richland, WA, 2007.

[170] F. Delbecq, Y. Wang, A. Muralidhara, K. El Ouardi, G. Marlair, C. Len, Hydrolysis of hemicellulose and derivatives—a review of recent advances in the production of furfural, Front. Chem. 6 (2018) 146.

[171] M. Audemar, C. Ciotonea, K. De Oliveira Vigier, S. Royer, A. Ungureanu, B. Dragoi, et al., Selective hydrogenation of furfural to furfuryl alcohol in the presence of a recyclable cobalt/SBA-15 catalyst, ChemSusChem 8 (2015) 1885−1891.

[172] Z. Zhang, K. Dong, Z.K. Zhao, Efficient conversion of furfuryl alcohol into alkyl levulinates catalyzed by an organic−inorganic hybrid solid acid catalyst, ChemSusChem 4 (2011) 112−118.

[173] D. Liu, D. Zemlyanov, T. Wu, R.J. Lobo-Lapidus, J.A. Dumesic, J.T. Miller, et al., Deactivation mechanistic studies of copper chromite catalyst for selective hydrogenation of 2-furfuraldehyde, J. Catal. 299 (2013) 336−345.

[174] Y. Wang, D. Zhao, D. Rodríguez-Padrón, C. Len, Recent advances in catalytic hydrogenation of furfural, Catalysts 9 (2019) 796.

[175] H. Chen, H. Ruan, X. Lu, J. Fu, T. Langrish, X. Lu, Efficient catalytic transfer hydrogenation of furfural to furfuryl alcohol in near-critical isopropanol over Cu/MgO-Al_2O_3 catalyst, Mol. Catal. 445 (2018) 94−101.

[176] J. Chen, W. Sun, Y. Wang, W. Fang, Performant Au hydrogenation catalyst cooperated with Cu-doped Al_2O_3 for selective conversion of furfural to furfuryl alcohol at ambient pressure, Green. Energy Environ. (2020). Available from: https://doi.org/10.1016/j.gee.2020.05.005.

[177] Y. Shi, Y. Zhu, Y. Yang, Y.-W. Li, H. Jiao, Exploring furfural catalytic conversion on Cu (111) from computation, ACS Catal. 5 (2015) 4020−4032.

[178] M.J. Islam, M. GranollersMesa, A. Osatiashtiani, M.J. Taylor, J.C. Manayil, C.M. Parlett, et al., The effect of metal precursor on copper phase dispersion and nanoparticle formation for the catalytic transformations of furfural, Appl. Catal. B: Environ. 273 (2020) 119062.

[179] Z. Shao, C. Li, X. Di, Z. Xiao, C. Liang, Aqueous-phase hydrogenation of succinic acid to γ-butyrolactone and tetrahydrofuran over Pd/C, Re/C, and Pd−Re/C catalysts, Ind. Eng. Chem. Res. 53 (2014) 9638−9645.

[180] S.D. Le, S. Nishimura, Highly selective synthesis of 1, 4-butanediol via hydrogenation of succinic acid with supported Cu−Pd alloy nanoparticles, ACS Sustain. Chem. Eng. 7 (2019) 18483−18492.

[181] A. Mazière, P. Prinsen, A. García, R. Luque, C. Len, A review of progress in (bio) catalytic routes from/to renewable succinic acid, Biofuels, Bioprod. Bioref. 11 (2017) 908−931.

[182] I. Bechthold, K. Bretz, S. Kabasci, R. Kopitzky, A. Springer, Succinic acid: a new platform chemical for biobased polymers from renewable resources, Chem. Eng. & Technol.: Ind. Chem. Plant. Equip. Process. Eng. Biotechnol. 31 (2008) 647−654.

[183] U.R. Pillai, E. Sahle-Demessie, Selective hydrogenation of maleic anhydride to γ-butyrolactone over Pd/Al_2O_3 catalyst using supercritical CO_2 as solvent, Chem. Commun. (2002) 422−423.

[184] C. You, C. Zhang, L. Chen, Z. Qi, Highly dispersed palladium nanoclusters incorporated in amino-functionalized silica spheres for the selective hydrogenation of succinic acid to γ-butyrolactone, Appl. Organomet. Chem. 29 (2015) 653−660.

[185] X. Liu, X. Wang, G. Xu, Q. Liu, X. Mu, H. Liu, Tuning the catalytic selectivity in biomass-derived succinic acid hydrogenation on FeO_x-modified Pd catalysts, J. Mater. Chem. A 3 (2015) 23560−23569.

[186] U.G. Hong, S. Hwang, J.G. Seo, J. Lee, I.K. Song, Hydrogenation of succinic acid to γ-butyrolactone (GBL) over palladium catalyst supported on alumina xerogel: Effect of acid density of the catalyst, J. Ind. Eng. Chem. 17 (2011) 316−320.

[187] C. Zhang, L. Chen, H. Cheng, X. Zhu, Z. Qi, Atomically dispersed Pd catalysts for the selective hydrogenation of succinic acid to γ-butyrolactone, Catal. Today 276 (2016) 55−61.